

MIT Open Access Articles

Effect of pore size distribution on the desalination performance of the selective layer of nanoporous atomically-thin membranes

The MIT Faculty has made this article openly available. **Please share** how this access benefits you. Your story matters.

Citation: Chow, Chun-Man and Karnik, Rohit. 2023. "Effect of pore size distribution on the desalination performance of the selective layer of nanoporous atomically-thin membranes." Desalination, 561.

As Published: 10.1016/j.desal.2023.116645

Publisher: Elsevier BV

Persistent URL: <https://hdl.handle.net/1721.1/155293>

Version: Author's final manuscript: final author's manuscript post peer review, without publisher's formatting or copy editing

Terms of use: Creative Commons Attribution-Noncommercial-ShareAlike



Effect of pore size distribution on the desalination performance of the selective layer of nanoporous atomically-thin membranes

Chun-Man Chow,^a Rohit Karnik^{b*}

^aDepartment of Chemical Engineering, Massachusetts Institute of Technology, 25 Ames St, Cambridge, MA 02142, USA

^bDepartment of Mechanical Engineering, Massachusetts Institute of Technology, 77 Massachusetts Ave, Cambridge, MA 02139, USA

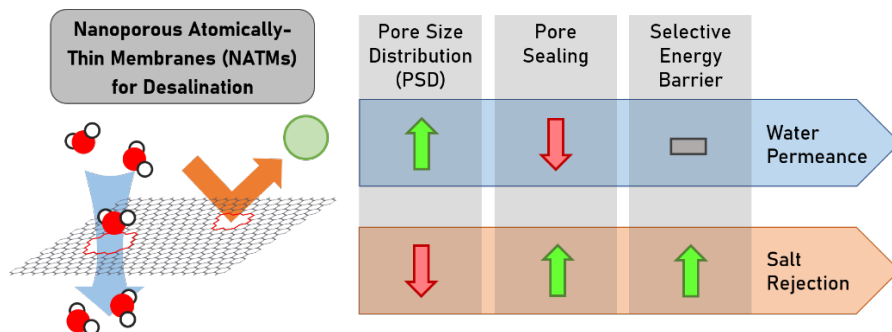
*Corresponding author: +1-617-324-1155, karnik@mit.edu

1. Abstract

Over the last decade, molecular simulations and experiments have shown that nanoporous atomically-thin membranes (NATMs) have the potential for high-permeance, high-selectivity separations, including seawater desalination. Realistic NATMs contain polydisperse pore sizes that could impede their performance, as large pores lead to salt leakage. This paper computationally examines the effect of pore size distributions (PSDs) on the desalination performance of the selective layer of NATMs by reverse osmosis (RO), considering size exclusion as the dominant selection mechanism. Analogous to thin-film composite RO membranes, the finite width of PSDs leads to a trade-off between water permeability and water/salt selectivity in NATMs. Tight PSDs with average pore sizes slightly below the size of the salt are needed to ensure high selectivity comparable to TFC membranes with high water permeance. Sealing of large, salt-permeable pores (e.g. by interfacial polymerization) limits salt leakage but substantially reduces water permeance. Introducing energy barriers that impede salt permeation by tuning nanopore structure and chemistry can make NATMs more robust to wider PSDs. In summary, some combination of control of PSDs, leakage mitigation, and pore functionalization is essential for NATMs to surpass the permeability/selectivity trade-off of polymeric RO membranes and achieve high water permeance with good salt rejection.

Keywords: Graphene, nanofluidics, reverse osmosis, pore flow, nanomaterial

Graphical Abstract:



2. Introduction

As water stress exacerbates due to climate change and population growth, desalination has become an attractive option to produce drinking water from an abundant source of water—the ocean—as well as other sources of saline water to augment water supply and complement the suite of solutions necessary to address the water crisis.¹ In its early days, desalination was achieved using thermal processes that evaporates the feed water and collects the steam that is free of salt. These continue to exist in the forms of multi-stage flash distillation or multiple-effect distillation with energy recovery incorporated to reduce energy consumption.²

However, today the majority of desalination is performed using reverse osmosis (RO) due to its cost-effectiveness and high energy efficiency.² Today's RO membranes are thin-film composite (TFC) polymer membranes typically made out of a polyamide active/selective layer, formed via interfacial polymerization of a diamine with a triacyl chloride, that blocks salt (at least to a great extent) and allows water to permeate through.² The selective layer is typically situated on top of a porous polysulfone support that provides mechanical strength, and the entire membrane is usually constructed as a spiral-wound module. Similar to other polymeric membranes, RO membranes face the trade-off between water permeability (or permeance) and water/salt selectivity, where permeability relates to how fast chemical species are able to pass through the membrane which governs its throughput and energy efficiency, and selectivity relates to how good the membrane is at rejecting salt. Typical water permeability for commercial seawater SWRO membranes is $\sim 3.5 \text{ m}^3 \text{ m}^{-2} \text{ Pa}^{-1} \text{ s}^{-1}$ ($1.3 \text{ L m}^{-2} \text{ h}^{-1} \text{ bar}^{-1}$) with salt rejection of 99.6-99.8%, and empirical evidence suggests that, with the same membrane material, it is difficult to raise water permeability without hurting selectivity,^{2,3} though active research is ongoing to push the permeability-selectivity upper bound via engineering ultra-thin membranes and/or incorporation of composite materials.^{4,5}

The emergence of 2D materials such as graphene, MoS₂, and hBN (hexagonal boron nitride) has opened up the possibility to create nanoporous atomically-thin membranes (NATMs). With an active layer of just one or a few atoms thick, they have potential as next-generation membranes that could push the upper bound of the permeability/selectivity trade-off by being extremely thin and enabling precise pore creation.⁶⁻⁹ However, current RO membranes with energy recovery processes incorporated already perform close to the thermodynamic limit in terms of specific energy consumption, and studies have shown that high permeance membranes do not yield substantial energy efficiency gains (>20%) by increasing permeance beyond $\sim 5 \text{ L m}^{-2} \text{ h}^{-1} \text{ bar}^{-1}$ for seawater.^{10,11} Nevertheless, high-permeance membranes could result in capital savings and allow for more compact membrane systems (e.g. lower pressure vessel requirements and smaller membrane area if fouling is not an issue), which could be useful in off-grid/decentralized applications, and also for the removal of chemical species from dilute streams such as in ultrapure water production or brackish water desalination because of the large volume of liquid that can be processed.¹⁰ In addition, because of its different separation mechanism compared to polymer membranes, 2D-membranes could potentially improve water/solute selectivity, which is a critical need for water treatment applications, especially in terms of rejecting small, neutral molecules.¹¹ Finally, the chemical and mechanical stability of 2D materials could enable these membranes to operate with harsh process streams or ultrahigh pressure differences, or lend itself to better cleaning and fouling control.^{12,13}

While previous studies have shown the tremendous potential of graphene and other atomically-thin materials as next-generation membrane materials in boosting permeance and selectivity, they usually focus on a single pore size or a small sub-set of pore sizes in estimating performance, drawing from molecular dynamics studies.^{6,14-16} A few experimental studies have also explored the desalination performance of nanoporous graphene composite membranes.^{9,17-19} Practical membranes, however, would have pore size distributions (PSDs) resulting from the pore creation and growth processes that would potentially compromise membrane performance via leakages through larger pores.¹⁸⁻²¹ How these PSDs affect desalination performance in terms of water permeance and salt rejection is important to further advancement of NATMs, but has not been systematically studied.

In this study, we use graphene as a model NATM to elucidate the transport behavior of water and salt (sodium chloride, NaCl) by using models that consider viscous fluid flow and salt diffusion and convection. Considering that the theoretical understanding of transport at the nanometer and subnanometer scale is still an active area of research,^{13,22} our model aims to capture qualitatively (and approximately quantitatively) the major, general behavior trends of NATM that arise at the practical scale using simplified models. This study examines the feasibility of realizing water desalination using NATMs with various PSDs, accounting for the effects of PSDs and leakage mitigation strategies on the membrane's performance. Study results could inform the design of future NATMs for water purification applications to address the growing demand for clean water.

3. Model development

Traditional polymeric RO membranes are modeled using a solution-diffusion model, where water and salt transport both occurs via diffusion driven by a concentration gradient.¹¹ Recently, Wang *et al.* presented a mechanistic solution-friction model that was able to capture the concentration and applied pressure-dependent salt permeability with water transported by hydraulic pressure gradient and salt transported via diffusion, advection, and electromigration.²³ In contrast, ultra- and micro- filtration literature adopts a pore-flow model that treats the polymer as a rigid, tortuous, porous network. A recent work by Hedge *et al.* illustrates that the solution-diffusion and pore-flow models are consistent with each other and describe the same phenomena, and provides a more extended fluid-solid model.²⁴ Here, we follow these previous works to use our mechanistic understanding of graphene transport to write continuum equations that could help us understand how realistically graphene membrane performs in desalination.

To make it easier to compare with traditional RO membranes, in addition to describing the flux behaviors, we also adopt metrics from the solution-diffusion model, particularly the water permeability coefficient (water permeance) A in $\text{L m}^{-2}\text{h}^{-1}\text{bar}^{-1}$, and the salt permeability coefficient (permeance) B in $\text{L m}^{-2}\text{h}^{-1} = 3.6 \times 10^6 \text{ m s}^{-1}$, even though the transport mechanisms are different across nanoporous graphene. We use subscripts w and s to indicate water and salt.

Similar to the solution-diffusion model, water flux J_w (volumetric flow rate per unit membrane area) is given by:

$$J_w = A [\Delta p - (1 - \xi_{g,w})\Delta\pi_m] = A[\Delta p - (1 - \xi_{g,w})\Delta\pi_b e^{J_w/k_f}] \quad (1)$$

where $A = P_w$ is the water permeance, Δp is the applied pressure difference, and $\xi_{g,w}$ is the fraction of graphene water permeance that contributes to salt leakage. The exponential term relates the osmotic pressure difference $\Delta\pi$ across the membrane m and across the bulk b to account for concentration polarization on the feed side, where salt builds up at the membrane surface. Unlike the solution-diffusion model for TFC membranes, there is an extra $(1 - \xi_{g,w})$ term in front of $\Delta\pi$ because osmotic pressure is null for the freely permeable part of the membrane. Details of the model derivation is included in **Appendix Section 8.1**. For membrane systems, salt concentration at the membrane surface on the feed side, $c_{f,m}$, is typically higher than the bulk feed side salt concentration $c_{f,b}$ due to concentration polarization, with k_f being the overall feed side mass transfer coefficient and c_p being the salt concentration on the permeate side.¹¹

$$\frac{\Delta c_m}{\Delta c_b} = \frac{c_{f,m} - c_p}{c_{f,b} - c_p} = \frac{\Delta\pi_m}{\Delta\pi_b} = e^{J_w/k_f}$$

$$c_{f,m} = c_{f,b} e^{J_w/k_f} - c_p (e^{J_w/k_f} - 1) = (c_{f,b} - c_p) e^{J_w/k_f} + c_p$$

Here, the equations are written for the more generalized case in the presence of concentration polarization. Our simulation in the main text, however, does not consider concentration polarization in order to focus on

the behavior of the nanoporous atomically-thin layer itself, as explained later in **Section 3.1**. The effects of concentration polarization are modeled and discussed in the **Appendix Section 8.5**.

The van't Hoff equation relates the osmotic pressure π and salt concentration c :

$$\pi = icR_gT \quad (2)$$

with van't Hoff factor $i = 2$ for sodium chloride. R_g and T are the ideal gas constant and temperature respectively.

3.1 Model for water and salt transport

The NATM of interest is made of a single-layer of nanoporous graphene on top of a porous support layer. The model is applicable to any NATM whose transport can be estimated using continuum equations, except when we consider energy barrier to salt transport across the pores in Section 3.4, where, while the energy parameters are specific to nanopore's structure and material, the framework is still generalizable. We use a resistance-in-series model to describe the graphene NATM permeance. Assuming there are only intentionally-created largely selective pores and no defects or tears on the graphene, we can write the overall membrane water permeance, which feeds into eq. (1), as:

$$A = P_w = \left[(\phi_s \rho_g P_{g,w}^{a>R_w})^{-1} + P_{supp,w}^{-1} \right]^{-1} \quad (3)$$

where ρ_g is the number density of nanopores (per unit area), $P_{g,w}^{a>R_w}$ is the water permeance over the graphene nanopores defined below, and $P_{supp,w}$ is the water permeance of the support. ϕ_s is the areal porosity of the surface of the support, and our model assumes that only the fraction ϕ_s of graphene that is suspended on the support pores conducts water and salt. All symbols are listed in the glossary.

Unlike water transport, the total salt flux, J_s , can be approximated as the sum of contributions from two mechanisms—convection and diffusion,²⁵ assuming the hydrated ion radius $R = 3.58 \text{ \AA}$ of Na^+ governs size exclusion (chlorine's hydrated ion radius is similar at 3.32 \AA)¹³ and neglecting any electrostatic/electrokinetic interactions:

$$\begin{aligned} J_s &= J_w c_p = J_{s,conv} + J_{s,diff} \\ J_{s,conv} &= J_w^{a>R} c_{f,m} = \xi_{g,w} P_w \left[\Delta p + (1 - \xi_{g,w}) \Delta \pi_m \left(\frac{\phi_s \rho_g P_{g,w}^{tot}}{P_{supp,w}} \right) \right] c_{f,m} \\ J_{s,diff} &= P_{diff} (c_{f,m} - c_p) \end{aligned} \quad (4)$$

Here, $J_{s,conv}$ is the convective salt flux, $J_w^{a>R}$ is the water flux through pores larger than the salt, and $J_{s,diff}$ is the salt flux by diffusion. The diffusive permeance is given by:

$$P_{diff} = \left[(\phi_s \rho_g P_{g,s}^{a>R})^{-1} + P_{supp,s}^{-1} \right]^{-1} \quad (5)$$

Eq. (4) can be compared to the salt flux in the solution-diffusion model, which assumes that diffusion is the main driving force:

$$J_s = B \Delta c_m \quad (6)$$

where B is the salt permeance.

As salt transport can be dominated by convection in the case of NATMs, we define an overall effective salt permeance P_s using the feed side concentration instead of the concentration difference to normalize the salt flux given that in most cases the feed side concentration is constant, whereas the permeate side concentration would be a function of the driving force Δp :

$$P_s \equiv \frac{J_s}{c_{f,b}} = \left[\xi_{g,w} P_w \left[\Delta p + (1 - \xi_{g,w}) \Delta \pi_m \left(\frac{\phi_s \rho_g P_{g,w}^{tot}}{P_{supp,w}} \right) \right] \frac{c_{f,m}}{c_{f,b}} + P_{diff} \left(\frac{c_{f,m}}{c_{f,b}} - \frac{c_p}{c_{f,b}} \right) e^{J_w/k_f} \right] \quad (7)$$

Defining P_s this way is analogous to B in the solution-diffusion model in eq. (6) and enables comparison of salt leakage across different membrane types.

To keep the problem tractable and generalizable, the water and salt permeances across the nanoporous graphene layer are estimated by assuming that (1) access resistance dominates the overall transport resistance (i.e. infinitely-thin membranes with no channel resistance; fluid transport can be modeled using Sampson flow as an approximation; see **Appendix Section 8.2** for details), (2) nanopores have negligible activation barrier for species translocation—only size exclusion affects transport (Section 3.4 relaxes this assumption by considering the effect of energy barrier) and could be described by continuum equations, i.e. single-pore permeance of $P_{g,w}(a) = a^3/3\mu$ for water flow and $P_{g,s}(a) = 2D(a - R)$ for salt diffusion, (3) the pores are circular and follow a pore size distribution (PSD) $f(a)$ where a is the radius of the pore (i.e. neglecting the jaggedness of the pores; alternatively “effective radius/diameters” could be used as is common in graphene literature),^{13,21,26–28} and (4) each pore’s transport can be treated independently such that there are no interactions between adjacent pores:

$$P_{g,w}^{a>R_w} = \int_{R_w}^{\infty} P_{g,w}(a) f(a) da = \frac{1}{3\mu} \int_{R_w}^{\infty} a^3 f(a) da \quad (8)$$

$$P_{g,w}^{a>R} = \int_R^{\infty} P_{g,w}(a) f(a) da = \frac{1}{3\mu} \int_R^{\infty} a^3 f(a) da \quad (9)$$

$$P_{g,s}^{a>R} = \int_R^{\infty} P_{g,s}(a) f(a) da = 2D \int_R^{\infty} (a - R) f(a) da \quad (10)$$

The fraction of graphene water permeance that contributes to salt leakage by convection is determined by taking the ratio between graphene water permeance for pores larger than the salt and overall graphene water permeance:

$$\xi_{g,w} = \frac{P_{g,w}^{a>R}}{P_{g,w}^{a>R_w}} < 1; \quad R > R_w \quad (11)$$

Here, as an approximation, we first assume size exclusion of the hydrated ion is the sole mechanism impeding salt transport, since that is cited to be the major contributor for ion rejection in nanoporous graphene membranes.¹⁶ We neglect any interactions between the salt ion and the pore and the possibility of ion dehydration,^{29–32} so as to focus on the effect of pore sizes on water and salt transport while keeping the problem tractable. Taking the hydration shell as a first approximation for the ion size is not unreasonable since the hydration free energy for Na^+ , $-411 \text{ kJ mol}^{-1} \sim -166 k_B T$ at 298 K, is significantly higher in magnitude than the thermal energy $k_B T$, where k_B is the Boltzmann constant and T is the temperature.³³ Although partial dehydration, i.e., shedding the first water molecule out of the average 5-6 water molecules in the first hydration shell of Na^+ , requires substantially less energy than removing successive water molecules, the interaction energy between Na^+ and the oxygen atom in the water molecule is $\sim -80 \text{ kJ mol}^{-1} \sim -32 k_B T$ at 298 K, which is quite high in magnitude,³⁴ suggesting that dehydration is likely not one of the primary mechanisms governing ion transport through nanopores, except in cases where the pores are smaller than the hydration size of the ion, at which point the ion transport rate would be significantly lower.³⁴ Nonetheless, we acknowledge that ions can pass through pores smaller than their hydrated ion radius, albeit at a low rate, and graphene pore edges could stabilize the partially dehydrated ion; however, the exact relationship between dehydration energy, pore size, pore chemistry, number of water removed, and ion type are not well known, with different MD studies giving varying energy values.^{16,35,36} These effects could be incorporated into our model as the literature’s understanding grows.

The access permeances predicted by the continuum models might differ somewhat from real permeances due to non-zero slip lengths and viscosity changes for nanometer and subnanometer pores of NATMs.³⁷ Nonetheless, based on molecular simulations, the difference is not more than an order of magnitude (e.g., $\sim 5\times$ for slip length of 1.5 nm),³⁷ and the insights drawn from using access resistance models should still

hold. Using continuum models enables rapid assessments of graphene performance, particularly with various pore sizes, without the need for computationally intensive molecule-level simulations.²⁸ Our framework can also be extended to other distributions (e.g. bimodal), pore shapes, or corrected for pore interactions with more accurate transport models, since the presence of functional groups could affect pore geometry, charge density, and friction experienced in the pore environment and thus affect water and salt transport—these effects require more extensive study beyond the scope of this paper,^{37–40} and the results will not be as generalizable. The electrostatic effects of these groups are considered in the energy barrier model presented in Section 3.4.

If $f(a)$ is lognormal (which is a reasonable approximation of pores created via some top-down methods e.g. focused ion beam, oxidative etching)^{18,19,26,41–43} with mean and standard deviation in log-space m and s (median: e^m ; see **Appendix Section 8.3** for more details on the use of lognormal curves to describe PSDs of experimentally fabricated membranes in literature), then analytical expressions can be written for the integrals in eq. (8)-(10):

$$P_{g,w}^{a>R} = \frac{1}{6\mu} e^{3m+9s^2/2} \operatorname{erfc} \left[\frac{\ln R - (m+3s^2)}{\sqrt{2}s} \right] \quad (12)$$

$$P_{g,s}^{a>R} = D \left(e^{m+s^2/2} \operatorname{erfc} \left[\frac{\ln R - (m+s^2)}{\sqrt{2}s} \right] - R \operatorname{erfc} \left[\frac{\ln R - m}{\sqrt{2}s} \right] \right) \quad (13)$$

3.2 Model parameters and solution

To focus our attention on the performance of the porous graphene layer itself, we impose a somewhat practical yet idealized support with low resistance to transport, with a constant and high water permeance $P_{supp,w} \sim 10^4 \text{ L m}^{-2} \text{ h}^{-1} \text{ bar}^{-1}$ ($= \phi_s a_s^2 / (8\mu L_s)$), a constant and very high sodium chloride diffusive permeance $P_{supp,s} \sim 10^{-3} \text{ m s}^{-1}$ ($= \phi_s D / L_s$), and porosity $\phi_s = 0.5$, without considering any specific membrane structure to isolate defects or maximize water permeance. A support with high water permeance would lead to low overall water/salt selectivity if the selective layer is leaky. However, the effect of support structure and resistance has been studied elsewhere,^{44–46} and a high support permeance to water allows us to elucidate the properties of the selective nanoporous graphene layer largely independent of the support. Similarly, we neglect concentration polarization to focus on the intrinsic properties of the nanoporous graphene selective layer independent of external flow parameters. In all cases, the feed salt concentration was assumed to be 0.6 M NaCl, and the pressure difference across the membrane was held constant at $\Delta p = 55.15 \text{ bar}$. **Table 1** summarizes the parameters used in the simulation.

In the absence of concentration polarization, we can substitute $c_{f,m} = c_{f,b} = c_f$ into the salt balance in eq. (4), which yields:

$$J_w c_p = \xi_{g,w} P_w \Delta p \left[1 + \left(1 - \frac{J_w}{\Delta p P_w} \right) \left(\frac{\phi_s \rho_g P_{g,w}^{tot}}{P_{supp,w}} \right) \right] c_f + P_{diff} (c_f - c_p) \quad (14)$$

Substituting in the expressions for $c_p(J_w)$ by rearranging eq. (1) and π from eq. (2) gives a single expression where J_w could be found by taking the ‘+’ root of a quadratic equation. The water flux J_w is then used to calculate the permeate concentration c_p using the rearranged eq. (1)-(2), the convective, diffusive, total salt fluxes $J_{s,conv}$, $J_{s,diff}$, J_s using eq. (4), and the overall effective salt permeance P_s using eq. (7), given the water and diffusive salt permeances P_w , $P_w^{a>R}$, and P_{diff} which can be determined independent of J_w or c_p as a function of the PSD parameters m and s . Details on the derivation is presented in **Appendix Section 8.1**.

The rejection by the membrane is given by:

$$\mathcal{R} = 1 - \frac{c_p}{c_{f,b}} = 1 - \tilde{c}_p \quad (15)$$

Table 1. Key variables and parameters in the desalination model.

Type	Parameter	Value	Description
Support	a_s	20 nm	Pore radius
	L_s	1 μm	Effective thickness (including tortuosity)
	ϕ_s	0.50	Porosity
Graphene	m	$\ln(0.05\text{-}0.5 \text{ [nm]})$	$\ln(\text{median pore radius})$ of graphene
	s	0-1.2	Standard deviation in log-space of PSD
	ρ_g	10^{16} m^{-2}	Graphene pore density
Constants	D	$1.62 \times 10^{-9} \text{ m}^2\text{s}^{-1}$	Sodium chloride NaCl diffusivity ²⁰
	R	3.58 \AA	Hydration radius of Na^{+13}
	R_w	0.839 \AA	Radius of the smallest cross-section area for water $\sim (0.73 + 0.64) \cos(52.237^\circ)$
	T	298 K	Temperature
	μ	$8.9 \times 10^{-4} \text{ Pa s}^{-1}$	Water viscosity
Operation	$c_{f,b}$	0.60 M	NaCl bulk feed concentration (seawater) ¹¹
	Δp	55.15 bar	Applied pressure ¹¹

3.3 Pore sealing

To further improve salt rejection and selectivity for water over salt, one can control the nanopore size distributions by completely sealing pores with radii above a cut-off, R_{cap} , e.g. through interfacial polymerization, atomic layer deposition (ALD), crosslinking, etc.^{17,20,47}, to block off flow through large pores that contribute to salt leakages.

We assume complete sealing of pores of $a > R_{cap}$, such that no water or salt can pass through those pores. The water and salt permeances in eq. (8)-(10) are then given by:

$$P_{g,w}^{R \rightarrow R_{cap}} = \int_{R_w}^{R_{cap}} P_{g,w}(a) f(a) da = \frac{1}{3\mu} \int_{R_w}^{R_{cap}} a^3 f(a) da \quad (16)$$

$$P_{g,w}^{R \rightarrow R_{cap}} = \int_R^{R_{cap}} P_{g,w}(a) f(a) da = \frac{1}{3\mu} \int_R^{R_{cap}} a^3 f(a) da \quad (17)$$

$$P_{g,s}^{R \rightarrow R_{cap}} = \int_R^{R_{cap}} P_{g,s}(a) f(a) da = 2D \int_R^{R_{cap}} (a - R) f(a) da \quad (18)$$

The rest of the equations follow as before. We examined R_{cap} values right below (0.3, 0.35 nm) and above (1.01R, 1.2R) the salt size, $R = 0.358 \text{ nm}$.

3.4 Energy barrier for salt transport

In the previous sections, we considered size exclusion as the sole mechanism for salt rejection.²⁸ We assumed that, unlike polymeric membranes or membranes with long channels, ion “solvation” into the graphene pore will be minimal because of its extreme thinness.⁴⁸ Here, we generalize the ion transport process to allow for the presence of energy barriers, where salt transport across the graphene pore can be treated as an Arrhenius-type, activated transport process overcoming an energy barrier, E_a , with E_a attributed to the interaction of the ion with the pore and the change in solvation environment around the ion due to the pore.⁴⁹ To examine the effect of such an energy barrier, which is likely to be dependent on pore size, we assume that there exists a type of barrier that only affects salt but not water. While we acknowledge that such a perfectly-selective energy barrier is unlikely to exist in real life—since realistically the transport of water and salt molecules for these small pores would both be affected by the presence of any functional groups on the pore edges—such an assumption enables us to estimate the upper bound of permselectivity that could be possible to achieve with the introduction of energy barriers, while keeping the model generalizable across pore types and sizes. As an approximation, we adjust the rates of salt transport equally for convection and diffusion by the same exponential factor:

$$P_{g,w}^{a>R} := P_{g,w}^{a>R} \exp\left(-\frac{E_a(a)}{k_B T}\right) \quad , \quad P_{g,s}^{a>R} := P_{g,s}^{a>R} \exp\left(-\frac{E_a(a)}{k_B T}\right) \quad (19)$$

where k_B is the Boltzmann constant and T is the temperature. These pore size-dependent permeances can be integrated across the pore size distribution $f(a)$ to yield the overall graphene permeances for salt as in eq. (9)-(10).

Following the literature,^{16,30,32,50–52} the energy barrier faced by the salt ion can be approximated by the sum of van der Waals (Lennard-Jones, E_{LJ}), electrostatic (E_{ES}), and dielectric exclusion components (E_{DE} could include Born energy $E_{DE,Born}$ and image forces $E_{DE,im}$).⁵³ If we assume that the van der Waals radius is already accounted for in defining the pore size, we can neglect the Lennard-Jones energy term E_{LJ} . Thus, we have:

$$E_a \approx E_{ES} + E_{DE} \quad (20)$$

We assume an electrostatic potential E_{ES} that is governed by the charges of the pore edge atoms and the ion, z_j and z_i , respectively, the atom-ion distance of $k_{ES,ij} a$ that is on the order of a , and the relative permittivity inside the pore ϵ_p . The dielectric Born energy $E_{DE,Born}$ considers the change in permittivity between the bulk and the pore, with the pore cavity size $k_{Born} a$ that is also on the order of a . The dielectric image force energy $E_{DE,im}$ results from the dielectric mismatch between the confined electrolyte ϵ_p and the membrane material (graphene) ϵ_g that leads to repulsive surface polarization. Thus, we have:

$$\begin{aligned} E_{ES} &\approx \frac{e^2}{4\pi\epsilon_0\epsilon_p(a)} \sum_j \frac{z_i z_j}{k_{ES,ij} a} \\ E_{DE,Born} &\approx \frac{e^2}{8\pi\epsilon_0} \frac{z_i^2}{k_{Born} a} \left(\frac{1}{\epsilon_p(a)} - \frac{1}{\epsilon_w} \right) \\ E_{DE,im} &\approx \frac{e^2}{8\pi\epsilon_0\epsilon_p(a)} \frac{z_i^2}{a} h(\epsilon_g, \epsilon_p(a)) \end{aligned} \quad (21)$$

where the Coulomb constant is $1/(4\pi\epsilon_0) = 14.4 \text{ eV } \text{\AA}^{-1}$ with ϵ_0 as the vacuum permittivity. At 25°C, the thermal energy is $k_B T = 0.0257 \text{ eV}$ ($= 2.48 \text{ kJ mol}^{-1} = 0.59 \text{ kcal mol}^{-1}$) and the relative permittivity (dielectric constant) for bulk water is $\epsilon_w = 78.2$.⁵⁴ e is the charge of an electron. h is a function that depends on the pore geometry and the dielectrics of the confined electrolyte and membrane material.

As a first approximation, we have assumed that the energy barrier $E_a(a)$ scales as a^{-1} since the electrostatic potential E_{ES} , dielectric Born energy $E_{DE,Born}$, and dielectric image force energy $E_{DE,im}$ are all assumed to be proportional to the inverse of the pore radius a for ultra-thin membranes. Such an approximation is necessary because the precise water structure around and within the graphene nanopores and the charge screening/interactions have not been studied across a wide array of pores. We therefore lump all of these energy contributions into a single parameter k_E to focus on the effect of the energy barrier size (eq. (21)), assuming a reasonable relationship between energy barrier and pore size while acknowledging the heterogeneity in real systems. We can thus write:

$$\frac{E_a(a)}{k_B T} \approx \left(\frac{e^2}{4\pi\epsilon_0\epsilon_w} \right) \frac{1}{k_B T} \frac{k_E}{a} = (7.2) \frac{k_E}{a [\text{\AA}]} \Big|_{T=298 \text{ K}} \quad (22)$$

We vary k_E over a realistically expected range of values of 0, 1, and 10 to investigate the effect of the size of the energy barrier on salt transport, where $k_E = 0$ corresponds to the case where there is no energy barrier impeding transport. These energy barriers match closely in magnitude with those observed in molecular dynamics simulations for monovalent salt ions in nanopores/nanoslits (see **Appendix Section 8.4, Figure A5**).⁴⁹ Physically, k_E can be affected by the net number of ion-pore atom interactions weighted by charges (e.g. through functional groups at the pore), the geometry of the pore, the change in permittivity within the pore due to nano-confinement that affects the fluid structure and charge screening ($\epsilon_p/\epsilon_w \sim 2$ for a silica cylindrical nanopore with a 6 Å radius), the ratio of membrane material (graphene) to bulk permittivity ($\epsilon_w/\epsilon_g \sim 10$), etc.^{29,49,53,55–58} However, a molecular dynamics study for KCl transport across sub-5 nm graphene nanopores indicated that, unlike conventional nanofiltration membranes, size exclusion is still the dominant factor governing transport across graphene nanopores and not dielectric exclusion, likely because of graphene's thinness which reduces its ability to affect the dielectric environment.¹⁶

4. Results and discussion

Practically, nearly all methods to fabricate NATMs result in membranes that contain a pore size distribution (PSD) which governs the transport of chemical species across them. Considering lognormal PSDs defined by mean and standard deviation in log-space of m and s , respectively, as described above, PSDs with larger median pore radii e^m have higher water and salt (convective and diffusive) permeances and thus higher fluxes, since the access permeance of water flow and salt diffusive scales as a^3 and a , where a is the pore radius (eq. (8)-(10)). Even for the same e^m , the permeances increases as pore sizes spread out more (larger s) because the larger pores at the right tail end of the PSD contribute more to the transport (**Figure 1a-b,d-e**). The permeances reach a plateau at high s as the graphene permeances approach the support permeance, such that graphene is no longer the dominant resistance in the resistance-in-series model. The low salt permeation for PSDs with median $e^m < R = 3.58 \text{ \AA}$ is due to size exclusion, where most of the pores in the PSDs are still smaller than the salt ion, so salt cannot pass through the membrane (a-c,e). PSDs with median pore sizes larger than the size of the salt ($e^m = 4, 5 \text{ \AA} > R = 3.58 \text{ \AA}$) reject almost no salt ($c_p/c_f \sim 1$) as convection drives salt transport through most of the pores. The contribution of diffusion to salt transport is increasingly dominant at small s , as the pores at the larger end of the PSD start to allow salt to diffuse through when the water velocity is still relatively low (f). It then decreases at larger s as c_p approaches c_f , and thus the concentration gradient, which is the driving force for diffusion, drops to zero and salt transport is dominated by convection.

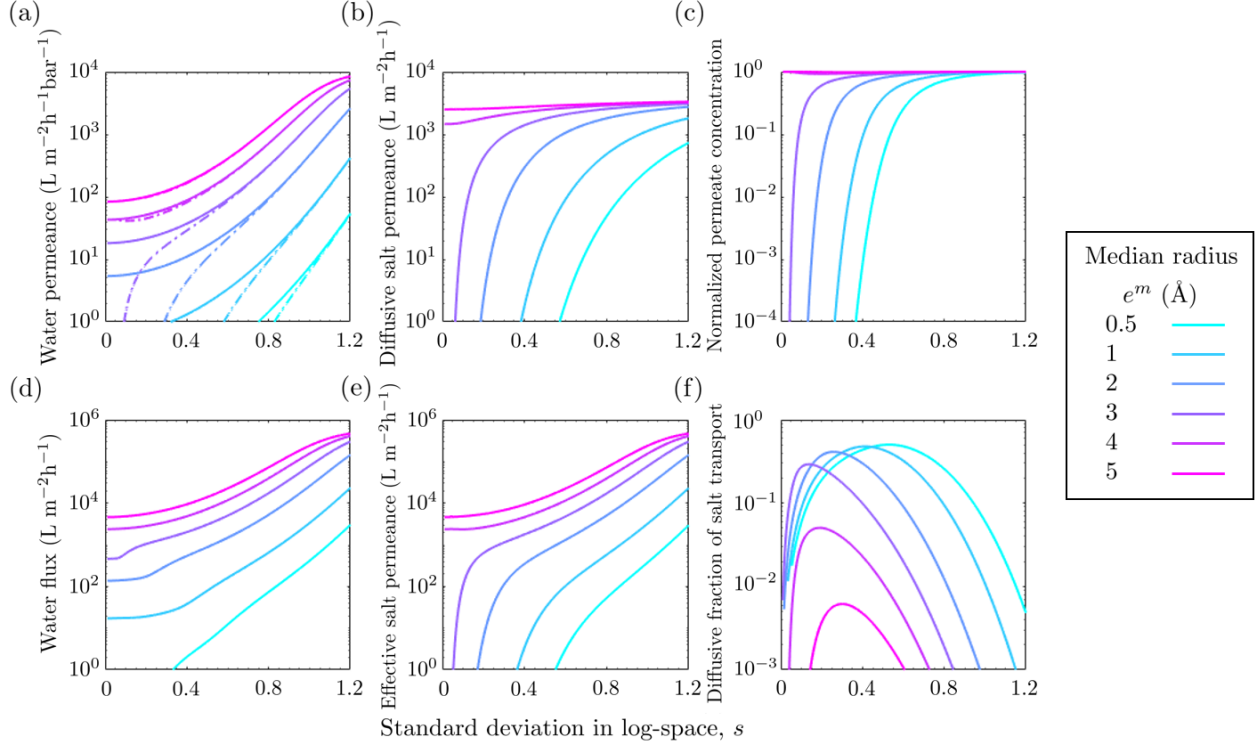


Figure 1. Effect of log-space standard deviation of lognormal PSDs, s (x-axis), and median pore radii e^m (denoted by different colors), on water and salt transport across the membrane. (a) Water permeance P_w (solid lines) and water permeance for pores larger than the salt $P_w^{a>R}$ (dot-dash lines). (b) Diffusive salt permeance P_{diff} . (c) Permeate salt concentration normalized by the feed concentration $\tilde{c}_p = c_p/c_f$. (d) Water flux, J_w . (e) Overall effective salt permeance, $P_s \equiv J_s/c_f$. (f) Diffusive fraction of the total salt flux J_{diff}/J_s .

Unlike membranes governed by the solution-diffusion mechanism where salt transport occurs mostly through diffusion and thus an increase in water flux dilutes the permeate stream,¹¹ because of convection-driven salt transport in NATMs, the permeate actually becomes more concentrated when the increase in water flux arises from pores larger than the hydrated ion size. The resultant adverse impact on membrane performance at large s can be seen in **Figure 2**, which plots the phase portraits of the membrane performance, with salt-related parameters on the vertical axes and water permeance on the horizontal axis. These diagrams enable us to visualize the relationship between water permeance and water/salt selectivity. It is seen that trade-off between water permeance and water/salt selectivity also arises in NATMs when we consider finite pore size distributions as a consequence of the increase in water permeance with pore size, and salt diffusion and convection through pores larger than the size of salt ions. The ideal membrane should block most of the salt while allowing high water flux, i.e. moving towards the top right corner in (b-d).

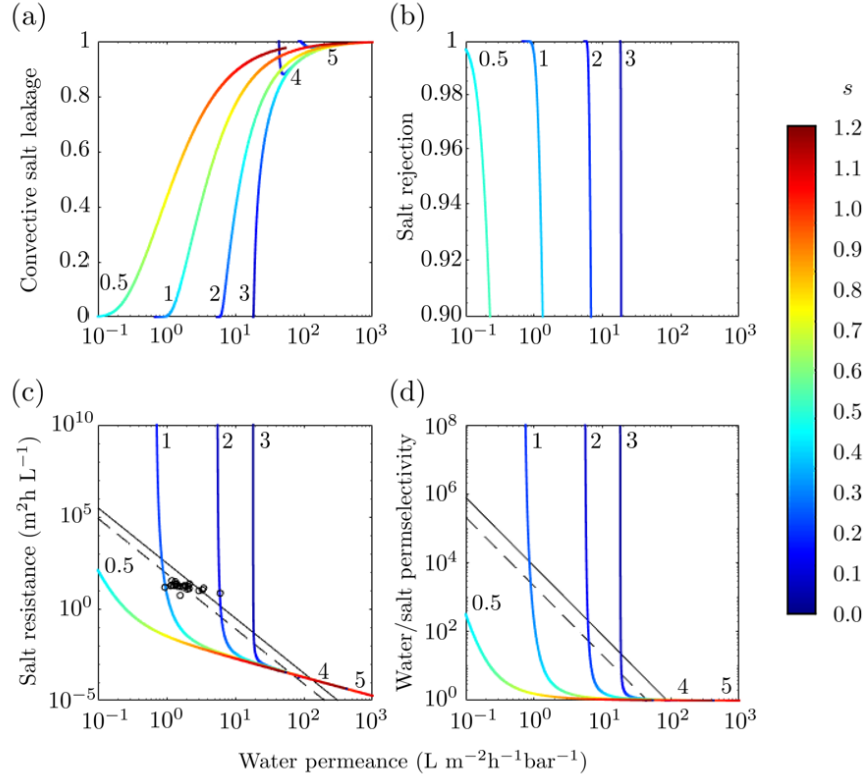


Figure 2. Phase portraits of the trade-off between different measures of salt transport against the water permeance P_w (x-axis) for different lognormal PSDs characterized by median pore radii e^m (values in Å indicated next to each curve) and standard deviation in log-space, s (denoted by color). (a) Convective salt leakage, defined as the ratio of water flux due to pores larger than the salt to the total water flux, $J_w^{a>R}/J_w$. (b) Salt rejection, given by $\mathcal{R} = 1 - c_p/c_f$. (c) Salt resistance (inverse of the effective salt permeance, $P_s \equiv J_s/c_f$, analogous to B^{-1} in the solution-diffusion model). The black dots denote B^{-1} versus A of commercial seawater RO membranes based on manufacturer technical specifications.¹¹ (d) Water/salt permselectivity, given by the ratio of the water flux to the salt permeance ($J_w/P_s = c_f/c_p$). The dash and solid black lines in (c-d) correspond to the empirically-determined and proposed upper bound permeance/selective trade-off curves for the membrane active layer of state-of-the-art, thin-film composite (TFC) polyamide membranes.^{11,59} Note that this upper bound could potentially be pushed higher (in the top right direction) by making the selective layer in TFC ultra-thin and incorporating composite materials, which is an area of active research.^{4,5}

As shown in **Figure 2a**, high water permeance with increasing spread of the PSDs (increasing s) is associated with high leakage via convection, $P_w^{a>R}/P_w$. For PSDs with medians smaller than the salt radius $e^m < R$, the leakage is initially 0 at low s , and rises as the tail ends of the PSDs exceed R , eventually becoming 1. All of these median pore size could reach salt rejection of >0.99 based on size exclusion mechanism alone, but only at small s (approximately less than $[0.4, 0.3, 0.2, 0.1]$ for $e^m = [0.5, 1, 2, 3]$ Å), as seen in **Figure 2b**. For PSDs with medians larger than R , the leakage is substantial even at small s , and rejection can never reach >0.9 . In these cases, salt rejection, salt transport resistance, and permselectivity drops extremely rapidly with the slightest increase in P_w (b-d). Therefore, to be above the proposed polymer permeance/selectivity upper bound, the NATMs need to have pores that are slightly smaller than R with tight PSDs, e.g. approximately $s < [0.3, 0.2, 0.1]$ for pore median $e^m = [1, 2, 3]$ Å, respectively. Assuming

that the continuum equation gives a reasonable estimate of transport rates, the water permeances achievable given the need to maintain high permselectivity could be significantly lower than the $\sim 100\text{-}1000 \text{ L m}^{-2}\text{h}^{-1}\text{bar}^{-1}$ proposed by molecular simulation studies due to the presence of PSDs.^{6,60}

It is important to note that the above permeance is based on two major assumptions: (1) a pore density $\rho_g = 10^{16} \text{ m}^{-2}$, and (2) the access resistance equations hold. A pore density of an order of magnitude higher, i.e. $\rho_g = 10^{17} \text{ m}^{-2}$, may be achievable with improved pore creation techniques, which would shift the water permeance by almost an order of magnitude higher. Recent theoretical work has also shown that the Sampson model could underestimate permeance by up to $\sim 5\times$ for small pores. Nonetheless, the insights from our study still hold—we have shown that near-perfect selectivity could be achieved with tight PSD without pore modifications, with water permeance higher than the typical permeance of existing seawater RO membranes ($1.3 \text{ L m}^{-2}\text{h}^{-1}\text{bar}^{-1}$).¹¹

4.1 Pore sealing

Next, we examined if sealing pores could yield better selectivity for NATMs, where the seal could be formed using methods such as interfacial polymerization, crosslinking, or atomic layer deposition.^{17,20,47} Pores that are larger than the sealant would be plugged. For seals where the cut-off radius is smaller than the hydrated ion size, $R_{cap} < R$, if size exclusion is the only mechanism limiting salt transport, then perfect selectivity is achievable (i.e., no salt permeation). However, unlike the no-sealing case, in the case of pore sealing, water permeance P_w can actually decrease with increasing s or e^m when a larger fraction of pores with radius $a > R_{cap}$ becomes plugged and impermeable (**Figure 3**). Therefore, for a given s , water permeance no longer increases monotonically with the median pore size e^m . For a given s , the water permeance P_w increases with e^m if $e^m \leq R_{cap}$, and falls with e^m if $e^m > R_{cap}$, where in the latter almost all the pores are sealed because they are larger than the sealing cut-off, R_{cap} . The highest water permeance corresponds to PSDs where the median pore radius e^m is right below R_{cap} with no spread in pore sizes ($s = 0$), with an R_{cap} right below the size of the salt. Yet, even the highest water permeance for the realistic PSDs and R_{cap} examined is well below $10^2 \text{ L m}^{-2}\text{h}^{-1}\text{bar}^{-1}$, suggesting that the price to pay for perfect selectivity via pore-sealing is a limited water permeance.

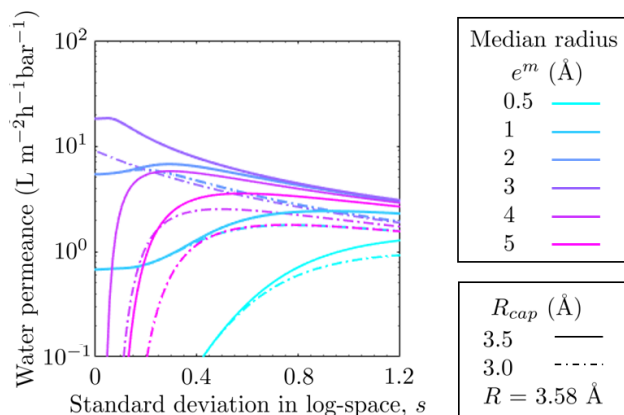


Figure 3. Water permeance P_w as a function of standard deviation in log-space s for different sealing cut-offs $R_{cap} = 3.5 \text{ Å}$ (solid) or $R_{cap} = 3.0 \text{ Å}$ (dot-dash), both of which are smaller than the salt ion radius $R = 3.58 \text{ Å}$. There is no salt transport since both cut-off values are below the salt ion size.

A more interesting case is when $R_{cap} > R$ where salt rejection is not perfect (**Figure 4**). Here, for a certain pore median where $e^m > R_{cap}$, physically plugging large non-selective pores reduces water permeation

more so than salt permeation as s increases, since the access permeance of water for a pore of radius a scales as a^3 whereas the diffusive salt permeance scales as a (Figure 4a-b). For $e^m < R_{cap}$, the water and salt permeances still rise with s for small s since the effect of introducing larger pores dominates over the effect of sealing of pores above the cutoff. The permeate salt concentration, water flux, and total salt permeance match with the behavior for water and diffusive salt permeance—for $e^m < R_{cap}$, these quantities increase with increasing s , whereas for $e^m > R_{cap}$, they eventually decrease with increasing s (Figure 4c-e). The diffusive contribution to the total salt flux behaves differently for pore-sealing vs. no-sealing. Here, the diffusive permeance increases sharply with s , and asymptotically approaches the same value for all median pore sizes, e^m . This value is higher for the larger cut-off, $R_{cap} = 1.2R$, because the sealing of the larger pores affects convection more so than diffusion due to the difference in the scaling of convective versus diffusive fluxes with pore size (a^3 versus a , respectively). Due to sealing of larger pores, convection no longer dominates salt transport at high s .

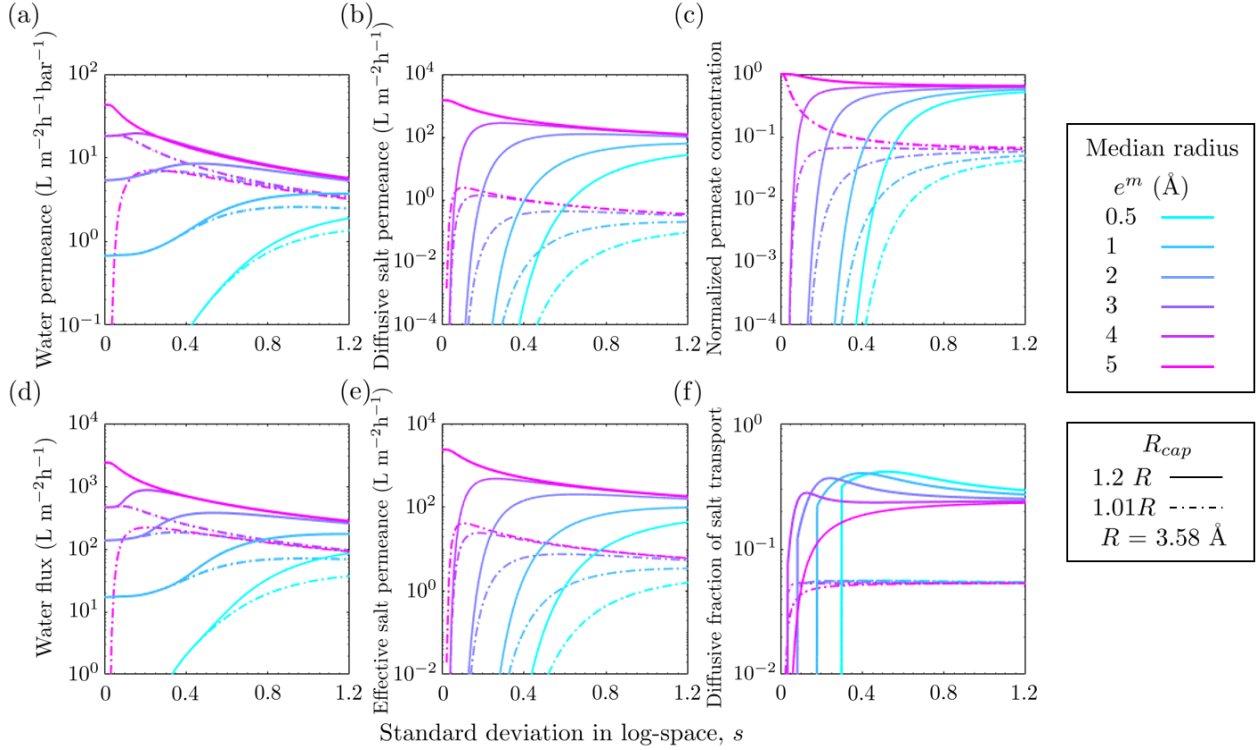


Figure 4. Effect of lognormal PSD parameters on water and salt transport for pore sealing cut-off (R_{cap}) values exceeding the salt size, with median pore size e^m as parameter (color) and standard deviation in log-space s , on the x-axis. (a) Water permeance, P_w . (b) Diffusive salt permeance, P_{diff} . (c) Normalized permeate salt concentration $\tilde{c}_p = c_p/c_f$. (d) Water flux, J_w . (e) Overall effective salt permeance, $P_s \equiv J_s/c_f$. (f) Diffusive contribution of the total salt flux, J_{diff}/J_s . $R_{cap} = 1.01R$ (solid lines) or $= 1.2R$ (dot-dash lines).

Figure 5a-b plots the phase portraits for permeate salt concentration (i.e., $1 - \text{salt rejection}$) and salt resistance against water permeance P_w for the $R_{cap} > R$ pore-sealing system. The behaviors for $e^m < R_{cap}$ are similar across the two R_{cap} values examined. For small e^m (0.5, 1 Å), as the PSD spread s increases, the water permeance P_w increases. Because the pores are small and mostly unsealed, salt rejection and salt transport resistance drop with increasing P_w . High rejection or high salt resistance is therefore only

achievable for low water permeances $P_w < 1 \text{ L m}^{-2} \text{ h}^{-1} \text{ bar}^{-1}$ for $e^m = 0.5$ and 1 \AA . For larger e^m still smaller than R ($2, 3 \text{ \AA}$), water permeance is already near its maximum at low s . It rises a little as s increases, which reduces salt rejection and salt resistance. With further increase in s beyond ~ 0.4 , the water permeance eventually decreases and drops lower than that at low values of s . The salt transport resistance, however, do not decrease towards 0 since $R_{cap} > R$ (**Figure 5b**); the salt transport resistance asymptotically reaches the same value of around 7×10^{-1} and $10^{-2} \text{ m}^2 \text{ h L}^{-1}$ at water permeance P_w of around 2 and $4 \text{ L m}^{-2} \text{ h}^{-1} \text{ bar}^{-1}$ for $R_{cap} = 1.01R$ and $1.2R$ with increasing s , respectively, both of which fall below the permeance/selectivity trade-off curve. This results in the “starfish” shaped curves in **Figure 5a-b**. For $e^m > R_{cap}$ (4 \AA), the system behaves differently between $R_{cap} = 1.01R$ and $1.2R$. For $R_{cap} = 1.01R$, at low s , as the PSD spread s increases, the water permeance P_w and salt rejection both increase, yet the salt transport resistance decreases; beyond $s = 0.3$, as s increases, salt rejection and salt transport resistance increase but the water permeance P_w decreases. In contrast, for $R_{cap} = 1.2R$, as s increases, water permeance and salt rejection both decrease monotonically and salt transport resistance increases. The results indicate, despite impeding water transport, pore sealing can prevent large leakage and enforce salt rejection and resistance to be above a threshold. However, pore sealing with large cut-offs ($R_{cap} > R$) is not able to push the performance substantially above the trade-off curve, and while pore sealing below the salt size ($R_{cap} < R$) achieves perfect selectivity, water permeance is limited (**Figure 3**).

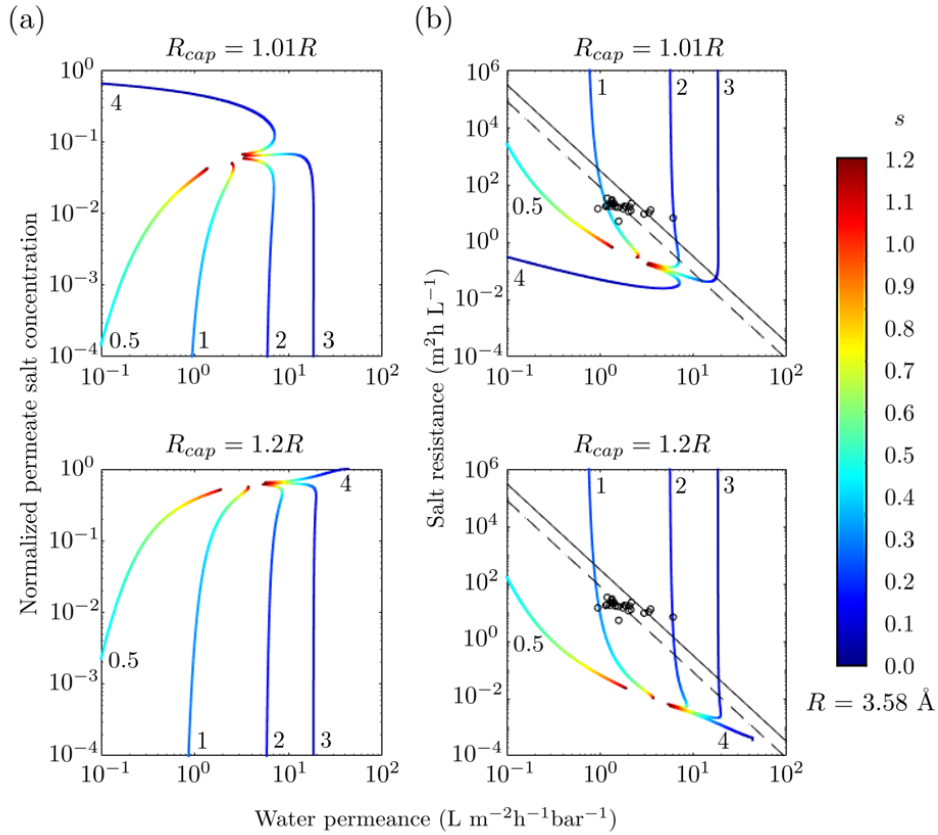


Figure 5. Phase portraits of the trade-off between different measures of salt transport against the water permeance P_w (x -axis) for different lognormal PSDs with pore sealing cut-offs $R_{cap} > R$ characterized by median pore radii e^m (values in \AA indicated next to each curve) and standard

deviation in log-space, s (denoted by color). (a) Permeate salt concentration normalized by the feed concentration $\tilde{c}_p = c_p/c_f = 1 - \mathcal{R}$, for $R_{cap} = 1.01R$ and $1.2R$. (b) Salt transport resistance (inverse of the effective salt permeance, P_s , for $R_{cap} = 1.01R$ and $1.2R$. The dash and solid black lines in (b) correspond to the empirically-determined and proposed upper bound permeance/selective trade-off curves for the membrane active layer of state-of-the-art, thin-film composite polyamide membranes.^{11,59}

4.2 Energy barrier for salt transport

Apart from size exclusion, NATM pores, particularly functionalized ones, could present an energy barrier for salt rejection. As discussed before, many of the sources of energy barrier imparted on the ion by the nanopore, including electrostatic and dielectric exclusion (Born energy and image forces), by approximation have the same pore size dependence of a^{-1} .⁵³ Here we tested the effect of different energy barrier heights $E_a = [e^2/4\pi\epsilon_0\epsilon_w] k_E/a$, with $k_E = 0, 1, 10$, on salt transport.

Figure 6 shows that the presence of an energy barrier for salt transport shifts the salt diffusive and total permeance curves lower, though not substantially unless the barrier exceeds the thermal energy, i.e., $E_a > k_B T$ or $k_E \gg 1$ (**Figure 6a,d**). This suggests that the change in permittivity of the environment as the salt ion enters the pore from the bulk, $\epsilon_p^{-1} - \epsilon_w^{-1}$, or the net sum of pore-ion charge interactions, $\sum_j z_i z_j$, have to be at least approximately half an order of magnitude for the energy barrier to be effective in limiting salt transport. The effect of the energy barrier on the salt permeance is the highest at low s since the energy barrier scales as the inverse of pore size a^{-1} , so the barrier approaches ∞ at small a/R , resulting in almost no salt permeation when only a few of the pores are large. This leads to a lower permeate salt concentration at low s (**Figure 6b**), and thus slightly lower water flux as the osmotic pressure becomes higher for a given feed concentration (**Figure 6c**). The diffusive component of the total salt flux follows a similar trend, initially increasing with s , hitting a peak, and then decreasing at high s (**Figure 6e**). However, the inverted-U shape of the curve becomes wider with increasing barrier height k_E , i.e., the diffusive component's contribution does not diminish as quickly with increasing s , since the a and a^3 scaling of the diffusive and convective flux components both get masked by the exponential term $\exp(-ka^{-1})$, where k is a constant.

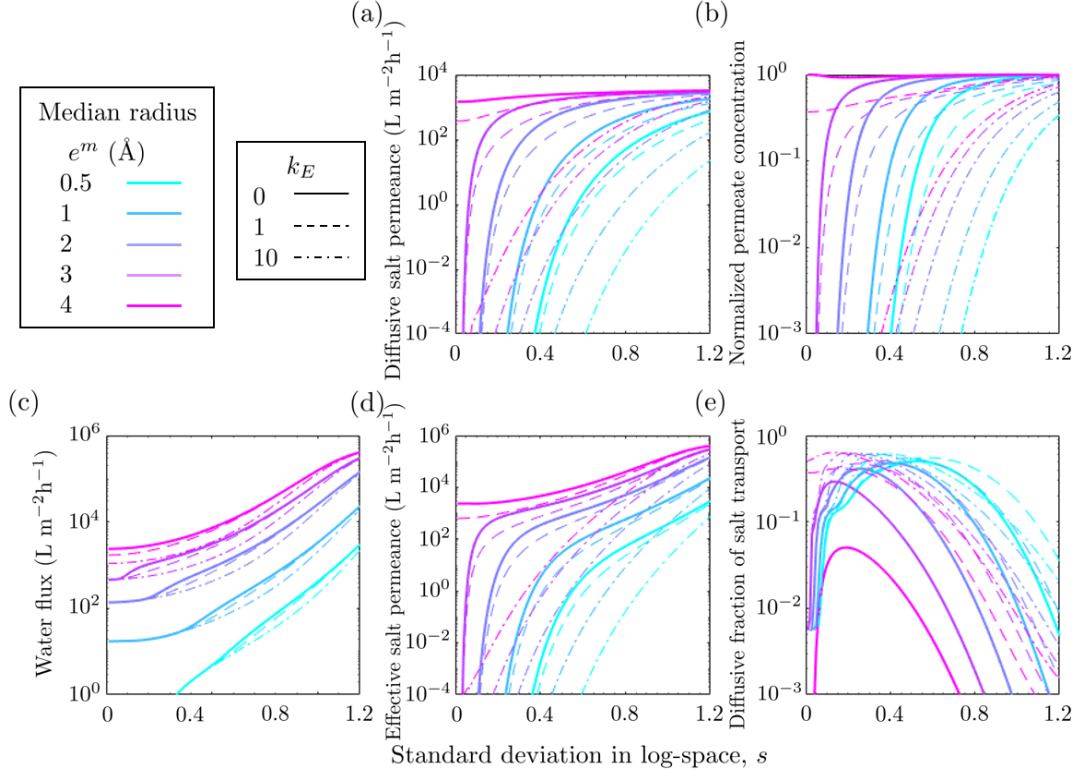


Figure 6. Effect of log-space standard deviation of lognormal PSDs, s (x -axis), and median pore radii e^m (denoted by different colors), on water and salt transport across the membrane in the presence of an energy barrier to salt transport parametrized by $k_E = 0$ (solid lines, no barrier), $k_E = 1$ (dash lines), and $k_E = 10$ (dot-dash lines). (a) Diffusive salt permeance, P_{diff} . (b) Permeate salt concentration normalized by the feed concentration $\tilde{c}_p = c_p/c_f$. (c) Water flux, J_w . (d) Overall effective salt permeance, $P_s \equiv J_s/c_f$. (e) Diffusive fraction of the total salt flux, J_{diff}/J_s .

The impact of the energy barrier height on the trade-off between water permeance and salt transport resistance is shown in **Figure 7** in the form of phase portraits. As before, higher water permeance that results from a wider spread of pore sizes at higher values of s is associated with lower salt rejection and salt transport resistance. A small energy barrier ($k_E = 1$) results in membrane behaviors that are similar to $k_E = 0$, with less than half an order of magnitude increase in salt rejection and resistance. In contrast, with $k_E = 10$, the salt rejection and salt transport resistance increase substantially beyond the polymer trade-off curve for all values of s , as long as the median pore sizes are large enough (i.e. $e^m > 1$ Å), although the distributions still have to be tight (small s) to ensure salt rejection is above 0.99. This implies that tuning the chemical structure of the pore could potentially overcome the leakage problem induced by wide PSDs and enable NATMs with broad PSDs to be used for desalination and ion separation purposes.

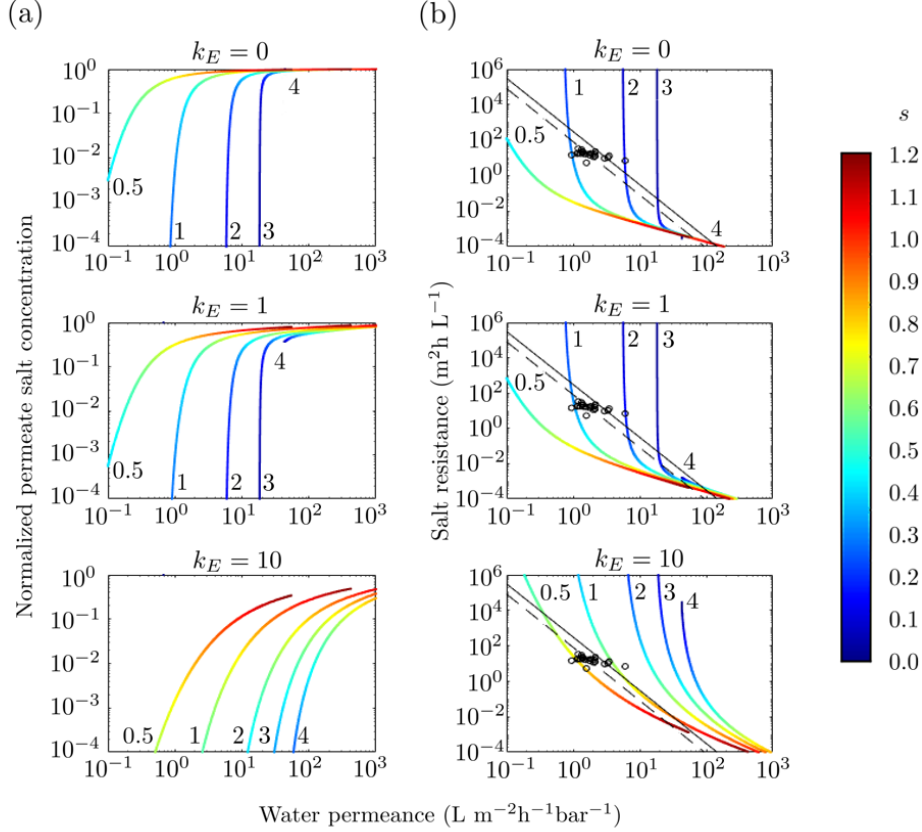


Figure 7. Phase portraits of the trade-off between different measures of salt transport against the water permeance P_w (x-axis) for different lognormal PSDs characterized by median pore radii e^m (values in Å indicated next to each curve) and standard deviation in log-space, s (denoted by color), in the presence of an energy barrier to salt transport parametrized by $k_E = 0, 1$, and 10 . (a) Permeate salt concentration normalized by the feed concentration $\tilde{c}_p = c_p/c_f = 1 - \mathcal{R}$. (b) Salt transport resistance (inverse of the effective salt permeance, P_s). The color indicates the log-space standard deviation of the PSD, s . The dash and solid black lines in (b) correspond to the empirically-determined and proposed upper bound permeance/selective trade-off curves for the membrane active layer of state-of-the-art, thin-film composite polyamide membranes.^{11,59}

5. Conclusion

Using nanoporous graphene as a model system, we have demonstrated that the selective nanoporous layer of nanoporous atomically-thin membranes with finite pore size distributions can yield performance beyond the upper limit of the permeance/water-salt selectivity trade-off curve of traditional polymeric thin-film composite RO membranes. Previous molecular simulation studies have mostly considered a single pore size in extracting graphene membrane performance, where, in order to maximize water permeance while maintaining selectivity, one should set the pore size to be right below the size cutoff. However, realistic membranes contain pores distributed across multiple sizes. If size exclusion is the dominant selection mechanism, then unmodified atomically-thin membranes can achieve high selectivity even with a finite spread in pore sizes, but the PSD has to be tight with small variance with median well below the hydrated ion size, especially since dehydration could also reduce the effective ion size that governs its transport. Although the water permeances across such selective graphene pores would still be higher than those of current polymeric RO membranes, they might not be as high as $100\text{-}1000 \text{ L m}^{-2}\text{h}^{-1}\text{bar}^{-1}$ predicted by previous studies due to engineering constraints, since the closer the pore sizes approach the hydrated ion

size, the higher the chance is for salt to leak, resulting in a water permeance versus selectivity trade-off that depends on the PSD parameters.

Our analysis illuminates the need for tight PSDs for achieving desalination, quantified by the spread, s , that is allowable for adequate salt transport resistance. Broad PSDs can severely impede the salt rejection as the tail ends of the distributions allow salt to leak through the membrane by convection, a phenomenon not as important in polymeric RO membranes where transport is relatively well-described by solution-diffusion. One method to address the broad PSD problem is to seal large pores to block off flow through them. Sealing all the pores that are around the size of or larger than the hydrated salt ion size, could in theory result in perfect salt rejection, but the water permeance would be limited and would even decrease as the PSDs broaden since a larger portion of the pores would be sealed. Hence pore sealing alone might not be ideal for resolving the leakage problem for broad PSDs.

Increasing the energy barrier experienced by the salt ion as it passes through the nanopore via tuning the pore structure and chemistry could be an effective way of mitigating salt leakage. Based on approximate pore size scaling for electrostatic and dielectric exclusion interactions, we demonstrated that the energy barrier has to be sufficiently large (e.g. $k_E \gg 1$) for the salt rejection and resistance to rise substantially. Large energy barriers could enable NATMs to surpass the permeance/selectivity trade-off limit of polymeric RO membranes even with wide PSDs provided the average pore sizes are not too small.

In conclusion, our study has shown that, similar to traditional polymeric membranes, nanoporous graphene membranes are subjected to the permeability/selectivity trade-off in desalination, and that size exclusion mechanisms could lead to desirable performance but are not robust against widening of pore size distributions, making NATMs unlikely candidates for practical desalination applications without strategies to mitigate leakage, such as sealing of leaky pores or tailoring of the porous support. In addition to these strategies, the present study shows that incorporating functional groups to adjust the pore structure and chemistry in NATMs may enable membranes derived from these materials to achieve better selectivity while maintaining high water permeance even in the case of broad pore size distributions. While future research could use more accurate/sophisticated transport models to improve the estimates of this work, the results and insights from this study could guide the development of practical NATMs to meet the rising water demand.

6. Acknowledgements

C.M.C. was supported by the National Science Foundation Graduate Research Fellowship under Grant No. 1745302 and the Croucher Foundation.

7. Glossary of symbols

Symbol	Description	Unit
a	Graphene pore radius	nm
a_s	Support pore radius	nm
$A = P_w$	Water permeability coefficient (water permeance)	$\text{L m}^{-2}\text{h}^{-1}\text{bar}^{-1}$
B	Salt permeability coefficient	$\text{L m}^{-2}\text{h}^{-1} = \text{m s}^{-1}$
$c_{f,j}$	Feed side NaCl concentration at bulk ($j = b$)/membrane surface ($j = m$)	M
c_p	NaCl permeate concentration	M
\tilde{c}_p	Normalized NaCl permeate concentration by bulk feed concentration	M
Δc_j	Concentration difference across the bulk ($j = b$)/membrane ($j = m$)	M
D	Sodium chloride NaCl diffusivity	m^2s^{-1}
e	Charge of an electron	C
E_a	Activation energy barrier for salt transport across graphene	J
E_j	Activation energy, $j = LJ$: Lennard-Jones (van der Waals), ES : Electrostatic, and DE : Dielectric exclusion	J
$f(a)$	Pore size distribution function	nm^{-1}
i	van't Hoff factor	-
$J_{diff}^{a>R}$	Diffusive salt flux for pores larger than NaCl	$\text{mol m}^{-2}\text{h}^{-1}$
J_s	Total salt flux	$\text{mol m}^{-2}\text{h}^{-1}$
$J_{s,conv}$	Salt flux by convective transport	$\text{mol m}^{-2}\text{h}^{-1}$
$J_{s,diff}$	Salt flux by diffusive transport	$\text{mol m}^{-2}\text{h}^{-1}$
J_w	Water flux	$\text{L m}^{-2}\text{h}^{-1}$
$J_w^{a>R}$	Water flux for pores larger than hydrated Na^+	$\text{L m}^{-2}\text{h}^{-1}$
k_B	Boltzmann constant	J K^{-1}
k_E	Activation energy constant	-
k_f	Overall feed side mass transfer coefficient	$\text{L m}^{-2}\text{h}^{-1}$
L_s	Support effective thickness (including tortuosity)	μm
m	Graphene: $\ln(\text{Median pore radius } [\text{nm}^{-1}])$	-
Δp	Applied pressure	bar
P_{diff}	Diffusive salt permeance	m s^{-1}
P_s	Overall effective salt permeance	m s^{-1}
$P_w = A$	Water permeability coefficient (water permeance)	$\text{L m}^{-2}\text{h}^{-1}\text{bar}^{-1}$
$P_w^{a>R}$	Water permeance for pores larger than NaCl	$\text{L m}^{-2}\text{h}^{-1}\text{bar}^{-1}$
$p_{g,s}^{a>R}$	Graphene diffusive salt permeance for pores larger than hydrated Na^+	m s^{-1}
$p_{g,w}^{a>R}$	Graphene water permeance for pores larger than hydrated Na^+	$\text{L m}^{-2}\text{h}^{-1}\text{bar}^{-1}$
$P_{supp,s}$	Support NaCl diffusive permeance	m s^{-1}
$P_{supp,w}$	Support water permeance	$\text{L m}^{-2}\text{h}^{-1}\text{bar}^{-1}$
R	Hydration radius of Na^+	\AA
\mathcal{R}	Salt rejection	-
R_{cap}	Pore radius cut-off	\AA
R_g	Ideal gas constant	$\text{J mol}^{-1}\text{K}^{-1}$
R_w	Radius of the smallest cross-section area for water	\AA
s	Graphene: Standard deviation in log-space of PSD	-
T	Temperature	K
z_i	Charge/valence of ion or functional group i	-
ϵ_0	Vacuum permittivity	F m^{-1}
ϵ_w	Relative permittivity (dielectric constant) for bulk water	F m^{-1}
μ	Water viscosity	Pa s^{-1}
$\xi_{g,w}$	Fraction of graphene water permeance that contributes to salt leakage	-
π	Osmotic pressure	bar
$\Delta\pi_b$	Osmotic pressure difference across the bulk ($j = b$)/ membrane ($j = m$)	bar
ϕ_s	Areal porosity of the surface of the support	-
ρ_g	Graphene pore density	m^{-2}

8. Appendix

8.1 Derivation of governing equations

As mentioned in the main text, the water flux cannot be written directly as $J_w = A (\Delta p - \Delta \pi_m)$ as in the solution-diffusion model because part of the graphene (the large pores that have negligible interaction with the ions) is freely permeable to salt, and thus the osmotic pressure there is null. The exact pore size at which a pore starts to interact with the salt ion is unknown; hence, as a first approximation we can assume, as in our size exclusion assumption, that pores are “freely permeable” to salt ions when they are larger than the salt ion, pores smaller than the salt ion are “semi permeable”, and the osmotic pressure adjustment in the water flux equation only applies to the latter. This “cut-off function” can be captured by a sigmoidal curve, $\alpha(a)$, where $\alpha(a \gg R) = 0$, and $\alpha(a \lesssim R) = 1$. For further simplicity, this curve is modeled as a step function with the step located at $a = R$.

For a membrane composite system with a support, one cannot just simply add the permeances together $(P_w - P_w^{a>R})(\Delta p - \Delta \pi_m) + P_w^{a>R} \Delta p$ to yield the water flux. To obtain the water flux equation, consider a 1D system with a pressure of $p_{f,m}$ and osmotic pressure of $\pi_{f,m}$ on the feed side of the graphene layer, p_{gs} and π_{gs} in the interface of graphene and support (assuming each support pore contains similar distributions of graphene nanopores), and p_p and π_p on the permeate side. For mass balance, water flux is the same across the support and graphene layers, noting that $\Delta \pi_m$ only applies to the semi-permeable part of the membrane:

$$J_w = P_{supp,w}(p_{gs} - p_p) = \phi_s \rho_g \int_{R_w}^{\infty} P_{g,w}(a) [p_{f,m} - p_{gs} - (\pi_{f,m} - \pi_{gs}) \alpha(a)] f(a) da \quad (23)$$

$$\approx \phi_s \rho_g P_{g,w}^{a>R} (p_{f,m} - p_{gs}) + \phi_s \rho_g P_{g,w}^{R_w \leq a \leq R} [p_{f,m} - p_{gs} - (\pi_{f,m} - \pi_{gs})]$$

where $\int_{R_w}^{\infty} P_{g,w}(a) \alpha(a) f(a) da \approx P_{g,w}^{R_w \leq a \leq R}$, i.e. only the semi-permeable part survives. For clarity we will use $P_{g,w}^{tot} = P_{g,w}^{a>R_w}$ interchangeably to indicate the total water permeance for the graphene membrane.

Rearranging to solve for p_{gs} :

$$p_{gs} = \frac{p_p P_{supp,w} + \phi_s \rho_g \int_{R_w}^{\infty} P_{g,w}(a) [p_{f,m} - (\pi_{f,m} - \pi_{gs})] \alpha(a) f(a) da}{P_{supp,w} + \phi_s \rho_g \int_{R_w}^{\infty} P_{g,w}(a) f(a) da}$$

$$p_{gs} = \frac{p_p P_{supp,w} + p_{f,m} \phi_s \rho_g \int_{R_w}^{\infty} P_{g,w}(a) \alpha(a) f(a) da - \phi_s \rho_g \int_{R_w}^{\infty} P_{g,w}(a) (\pi_{f,m} - \pi_{gs}) \alpha(a) f(a) da}{P_{supp,w} + \int_{R_w}^{\infty} P_{g,w}(a) f(a) da}$$

$$p_{gs} \approx \frac{p_p P_{supp,w} + p_{f,m} \phi_s \rho_g P_{g,w}^{tot} - (\pi_{f,m} - \pi_{gs}) \phi_s \rho_g (P_{g,w}^{tot} - P_{g,w}^{a>R})}{P_{supp,w} + \phi_s \rho_g P_{g,w}^{tot}}$$

Plugging p_{gs} into the J_w equation yields:

$$J_w = \frac{P_{supp,w} \phi_s \rho_g}{P_{supp,w} + \phi_s \rho_g P_{g,w}^{a>R_w}} [(p_{f,m} - p_p) P_{g,w}^{a>R_w} - (\pi_{f,m} - \pi_{gs}) (P_{g,w}^{a>R_w} - P_{g,w}^{a>R})]$$

$$J_w = \frac{[(p_{f,m} - p_p) - (P_{g,w}^{a>R_w})^{-1} \int_{R_w}^{\infty} P_{g,w}(a) (\pi_{f,m} - \pi_{gs}) \alpha(a) f(a) da]}{(\phi_s \rho_g P_{g,w}^{a>R_w})^{-1} + P_{supp,w}^{-1}} \approx \frac{(p_{f,m} - p_p) - (1 - \xi_{g,w}) (\pi_{f,m} - \pi_{gs})}{(\phi_s \rho_g P_{g,w}^{a>R_w})^{-1} + P_{supp,w}^{-1}}$$

where for clarity we define $\xi_{g,w}$ as the fraction of graphene water permeance that is contributing to salt leakage, $\xi_{g,w} = P_{g,w}^{a>R} / P_{g,w}^{tot}$. Given $P_w^{-1} = (\phi_s \rho_g P_{g,w}^{a>R_w})^{-1} + P_{supp,w}^{-1}$, we can write:

$$J_w = P_w [(p_{f,m} - p_p) - (P_{g,w}^{tot})^{-1} \int_{R_w}^{\infty} P_{g,w}(a) (\pi_{f,m} - \pi_{gs}) \alpha(a) f(a) da]$$

$$J_w \approx P_w [(p_{f,m} - p_p) - (1 - \xi_{g,w}) (\pi_{f,m} - \pi_{gs})]$$

We further assume $\pi_{gs} \approx \pi_p$ since the concentration gradient across the support is typically small relative to that across the graphene layer. We can also define P_w^{expt} as the “experimentally measured permeance” of this membrane composite:

$$J_w = P_w [\Delta p - (1 - \xi_{g,w}) \Delta \pi_m] = P_w^{expt} [\Delta p - \Delta \pi_m]$$

$$P_w^{expt} \approx P_w \left(1 + \xi_{g,w} \frac{\Delta \pi_m}{\Delta p - \Delta \pi_m} \right)$$

We see that P_w^{expt} will overestimate the true P_w as it assumes the osmotic pressure applies to all pores. We can also rearrange to write c_p (or \tilde{c}_p as the dimensionless form scaled by $c_{f,b}$) as a function of J_w :

$$J_w \approx P_w [\Delta p - (1 - \xi_{g,w}) i R_g T (c_{f,m} - c_p)] \quad (24)$$

$$\tilde{c}_p(J_w) = \tilde{c}_{f,m} - \frac{(1 - \xi_{g,w})^{-1}}{i R_g T c_{f,b}} \left(\Delta p - \frac{J_w}{P_w} \right) = 1 - \frac{\Delta p}{i R_g T c_{f,b}} (1 - \xi_{g,w})^{-1} \left(1 - \frac{J_w}{P_w \Delta p} \right) e^{-J_w/k_f} \quad (25)$$

The salt leakage part of the water flux to be used in the salt flux equation is:

$$J_w^{a>R} = \phi_s \rho_g P_{g,w}^{a>R} (p_{f,m} - p_{gs}) = \phi_s \rho_g P_{g,w}^{tot} \xi_{g,w} (p_{f,m} - p_{gs})$$

$$J_w^{a>R} = \phi_s \rho_g P_{g,w}^{tot} \xi_{g,w} \left(p_{f,m} - \frac{p_p P_{supp,w} + p_{f,m} \phi_s \rho_g P_{g,w}^{a>R} - \phi_s \rho_g \int_{R_w}^{\infty} P_{g,w}(a) (\pi_{f,m} - \pi_{gs}) \alpha(a) f(a) da}{P_{supp,w} + \phi_s \rho_g P_{g,w}^{a>R}} \right)$$

$$J_w^{a>R} = \frac{\phi_s \rho_g P_{g,w}^{tot}}{P_{supp,w} + \phi_s \rho_g P_{g,w}^{tot}} \xi_{g,w} [(p_{f,m} - p_p) P_{supp,w} + \phi_s \rho_g P_{g,w}^{tot} (1 - \xi_{g,w}) (\pi_{f,m} - \pi_{gs})]$$

$$J_w^{a>R} = \xi_{g,w} P_w \left[(p_{f,m} - p_p) + (1 - \xi_{g,w}) (\pi_{f,m} - \pi_{gs}) \left(\frac{\phi_s \rho_g P_{g,w}^{tot}}{P_{supp,w}} \right) \right]$$

$$J_w^{a>R} = \xi_{g,w} P_w \left[\Delta p + (1 - \xi_{g,w}) \Delta \pi_m \left(\frac{\phi_s \rho_g P_{g,w}^{tot}}{P_{supp,w}} \right) \right] \quad (26)$$

which increases as the leaky fraction of the graphene permeance, $\xi_{g,w}$, increases. Increasing osmotic pressure also increase $J_w^{a>R}$ because there is now a weaker driving for the semi-permeable pores ($\Delta p - \Delta \pi$), and thus water prefers to flow through the leaky pore. Decreasing support permeance (i.e. increasing support resistance) also amplifies the osmotic pressure contribution (noting that a decrease in $P_{supp,w}$ will decrease P_w) as the interfacial pressure p_{gs} shifts closer to the feed pressure p_f and away from the permeate pressure p_p , so osmotic pressure has a stronger effect on graphene as it is larger relative to the driving force over the graphene layer ($p_f - p_{gs}$).

Note that one can also write $J_w^{a>R}$ as a function of J_w by substituting in $\tilde{c}_p(J_w)$:

$$J_w^{a>R} = \xi_{g,w} P_w \left[\Delta p + (1 - \xi_{g,w}) i R_g T c_{f,b} (1 - \tilde{c}_p) e^{J_w/k_f} \left(\frac{\phi_s \rho_g P_{g,w}^{tot}}{P_{supp,w}} \right) \right]$$

$$J_w^{a>R} = \xi_{g,w} P_w \Delta p \left[1 + \left(1 - \frac{J_w}{\Delta p P_w} \right) \left(\frac{\phi_s \rho_g P_{g,w}^{tot}}{P_{supp,w}} \right) \right] \quad (27)$$

8.1.1 Numerical solution to the concentration polarization model

The solution for the case with concentration polarization is not as straightforward as finding the solution to solution-diffusion membrane systems, since in 2D membrane systems there is a coupling between convection and diffusion, where the former is driven by $c_{f,m}$ and the latter by $\Delta c_m = c_{f,m} - c_p$.

To find the water and salt fluxes and permeate concentration, we write one equation containing all known entities to solve for J_w , starting from the salt balance and substituting in expressions for $c_{f,m}$ (from the main text), c_p , and $J_w^{a>R}$:

$$\begin{aligned} J_s &= J_w c_p = J_w^{a>R} c_{f,m} + P_{diff} (c_{f,b} - c_p) e^{J_w/k_f} \\ J_w \tilde{c}_p &= J_w^{a>R} [e^{J_w/k_f} - \tilde{c}_p (e^{J_w/k_f} - 1)] + P_{diff} (1 - \tilde{c}_p) e^{J_w/k_f} \\ [J_w e^{-J_w/k_f} + J_w^{a>R} (1 - e^{-J_w/k_f}) + P_{diff}] \tilde{c}_p - (J_w^{a>R} + P_{diff}) &= 0 \end{aligned} \quad (28)$$

where for numerical stability we prefer e^{-J_w/k_f} over e^{J_w/k_f} . J_w from the solution of eq. (28) can be plugged back into eq. (25) and (27) to determine c_p and $J_w^{a>R}$, and the salt fluxes can then be determined.

8.1.2 Analytical solution to the model without concentration polarization

In the absence of concentration polarization, we can substitute $c_{f,m} = c_{f,b}$ into the salt balance, i.e. ignoring the e^{J_w/k_f} terms, which yields:

$$J_s = J_w c_p = J_w^{a>R} c_{f,b} + P_{diff} (c_{f,b} - c_p)$$

This allows us to solve for J_w using a single quadratic equation after substituting in the expressions $J_w^{a>R}(J_w)$ and $c_p(J_w)$:

$$\begin{aligned} J_w \left[1 - \frac{\Delta p}{i_{R_g} T c_{f,b}} (1 - \xi_{g,w})^{-1} \left(1 - \frac{J_w}{P_w \Delta p} \right) \right] &= \xi_{g,w} P_w \Delta p \left[1 + \left(1 - \frac{J_w}{\Delta p P_w} \right) \left(\frac{\phi_s \rho_g P_{g,w}^{tot}}{P_{supp,w}} \right) \right] + P_{diff} \left[\frac{\Delta p}{i_{R_g} T c_{f,b}} (1 - \xi_{g,w})^{-1} \left(1 - \frac{J_w}{P_w \Delta p} \right) \right] \\ J_w^2 \left[\frac{\Delta p}{i_{R_g} T c_{f,b}} (1 - \xi_{g,w})^{-1} \left(\frac{1}{P_w \Delta p} \right) \right] &+ J_w \left[1 - \frac{\Delta p}{i_{R_g} T c_{f,b}} (1 - \xi_{g,w})^{-1} + \xi_{g,w} \left(\frac{\phi_s \rho_g P_{g,w}^{tot}}{P_{supp,w}} \right) + P_{diff} \left(\frac{\Delta p}{i_{R_g} T c_{f,b}} (1 - \xi_{g,w})^{-1} \left(\frac{1}{P_w \Delta p} \right) \right) \right] \\ &- \left\{ \xi_{g,w} P_w \Delta p \left[1 + \left(\frac{\phi_s \rho_g P_{g,w}^{tot}}{P_{supp,w}} \right) \right] + P_{diff} \left(\frac{\Delta p}{i_{R_g} T c_{f,b}} (1 - \xi_{g,w})^{-1} \right) \right\} = 0 \\ J_w^2 + J_w (P_w \Delta p) \left\{ (1 - \xi_{g,w}) \left(\frac{i_{R_g} T c_{f,b}}{\Delta p} \right) \left[1 + \xi_{g,w} \left(\frac{\phi_s \rho_g P_{g,w}^{tot}}{P_{supp,w}} \right) \right] + \frac{P_{diff}}{P_w \Delta p} - 1 \right\} &- (P_w \Delta p)^2 \left\{ (1 - \xi_{g,w}) \xi_{g,w} \left(\frac{i_{R_g} T c_{f,b}}{\Delta p} \right) \left[1 + \left(\frac{\phi_s \rho_g P_{g,w}^{tot}}{P_{supp,w}} \right) \right] + \frac{P_{diff}}{P_w \Delta p} \right\} = 0 \end{aligned} \quad (29)$$

8.2 Molecular dynamics simulation informed continuum models for water flow across nanopores

More sophisticated continuum models have been developed in the recent years to describe water flow across nano and subnanometer pores. These models are more accurate than the Sampson and Dagan models that involves putting the entrance/exit resistance (Sampson) in series with the center-pore resistance (Hagen-Poiseuille),⁶¹ which were shown to underestimate flow across small pores (less than ~ 10 nm in radius) made from carbon molecules (e.g. graphene, carbon nanotubes CNTs). These models involve correcting for thermophysical parameters that affect water transport, e.g. viscosity μ and slip length δ_s (which can be expressed as viscosity/friction coefficient λ), in the pore vicinity which would differ from their bulk values due to interactions at the molecular length scale. Given experimental limitations, these parameters can be obtained from MD simulations via Green-Kubo relations, which relate these macroscopic properties with microscopic fluctuations.^{39,40}

8.2.1 Model development

Heiranian et al. proposed a correction to the Sampson equation, where the slip and viscosity corrected Sampson hydrodynamic resistance can be written as a linear combination of the slip-corrected and excess-viscosity-corrected resistance (i.e. treating them as resistances in series):³⁷

$$\frac{R_{\text{slip-visc}}^{\text{Sampson}}}{R^{\text{Sampson}}} = \frac{R_{\text{slip}}^{\text{Sampson}} + R_{\text{visc}}^{\text{Sampson}}}{R^{\text{Sampson}}} \quad (30)$$

$$= \frac{1 + 2 \left(\frac{\alpha}{1 + \alpha} \right)^{3/2} - 3 \left(\frac{\alpha}{1 + \alpha} \right)}{(1 + \alpha)^{3/2}} + \frac{2 \mu_{\text{excess}}}{\pi \mu} \left[\tan^{-1} \beta + \ln(\beta^{-2} + 1) \left(\frac{3}{2} \beta + \beta^3 \right) - \beta \right]$$

where $\alpha = \delta_s/a$ is the ratio of slip length to pore radius, with δ_s assumed to be 1.5 nm; $\beta = L_{\text{int}}/a$ is the ratio of interfacial layer thickness (distance from the graphene wall where most of the variations in viscosity take place) to pore radius, with L_{int} assumed to be 0.8 nm; $\mu_{\text{excess}} = 0.13$ mPa s is the average excess viscosity near the graphene-water interface. The corrected permeance is then:³⁷

$$P_{g,w}^{\text{slip-visc}}(a) = P_{g,w}(a) \left(\frac{R_{\text{slip-visc}}^{\text{Sampson}}}{R^{\text{Sampson}}} \right)^{-1} \quad (31)$$

In another paper, the same authors (Heiranian and Aluru) provides another method, which they coined the corrected Hagen-Poiseuille (CHP) model, to estimate water permeance:³⁹

$$P_{g,w}^{\text{CHP}}(a) = \frac{\pi \left(a^4 + \frac{4a^3 \mu(L_g, a)}{\lambda(L_g, a)} \right)}{8\mu(L_g, a)} \frac{1}{L_g^{\text{Dagan}}} = \frac{\pi a^3 (a + 4\delta_s(L_g, a))}{8\mu(L_g, a)(L_g + 3\pi a/8)} \quad (32)$$

where $L_g = 0.335$ nm is the graphene thickness and the effective hydrodynamic pressure drop length is $L_g^{\text{Dagan}} = L_g + (3\pi/8)a$. The viscosity, friction coefficient, and slip length δ_s 's dependence on pore radius a and pore length can be obtained via fitted functions to non-equilibrium molecular dynamics (NEMD) simulations. While the NEMD simulations were performed for both carbon nanotubes (CNTs) and graphene, the fitted equations provided in the paper were for CNTs, which show different behaviors vs. graphene (**Figure A1**).

Assuming the typical length of variation for the parameters is $x_e = 0.7$ nm from the edge of a nanotube/nanopore, the combined length of the end regions can be defined as $l = 2x_e(1 - e^{-L_g/2x_e}) = 1.4$ nm ($1 - e^{-3.35/14}$) ≈ 0.30 nm. The pore length and radius dependent viscosity μ and friction coefficient λ can be calculated as a weighted average of values in the end regions (μ^e, λ^e) and middle section ($\mu^\infty, \lambda^\infty$):

$$\mu(L_g, a) = \frac{l \cdot \mu^e(a) + (L_g - l)\mu^\infty(a)}{L_g} \quad (33)$$

$$\lambda(L_g, a) = \frac{l \cdot \lambda^e(a) + (L_g - l)\lambda^\infty(a)}{L_g} \quad (34)$$

with $\mu^e(a) = [(0.38 \text{ nm}/a)^2 - 2(0.38 \text{ nm}/a)](\mu - 9.5 \times 10^{-4} \text{ Pa s}) + \mu$, $\mu^\infty(a) = [(0.38 \text{ nm}/a)^2 - 2(0.38 \text{ nm}/a)](\mu - 3.2 \times 10^{-4} \text{ Pa s}) + \mu$, $\lambda^e(a) = (0.59[a/\text{nm}]^{-3.5} + 4.2) \times 10^5 \text{ N s m}^{-3}$, $\lambda^\infty(a) = (-0.63[a/\text{nm}]^{-0.6} + 1.1) \times 10^4 \text{ N s m}^{-3}$.

Similarly, Sun et al.⁴⁰ developed a nanoscale unified model of the same form as Heiranian and Aluru's CHP model,³⁹ accounting for the varying viscosity μ and slip length δ_s with pore radius a in the same Dagan-like Hagen-Poiseuille form (although the authors derived it differently):

$$P_{g,w}^{\text{NUM}}(a) = \frac{\pi a^3(a + 4\delta_s)}{8\mu(L_g + 3\pi a/8)} \quad (35)$$

However, similar to Heiranian and Aluru's paper, Sun et al.'s also did not explicitly define functions to describe the $\mu(a)$ and $\delta_s(a)$ for graphene. Here, using the MD data from the above papers, we fitted functional forms describing the pore size dependent of these thermophysical models to enable the calculation of water permeance across all a (**Table A1**).

Figure A1 shows that different MD simulations resulted in different values and pore size dependence for the parameters. Note that the CHP model provided in Heiranian and Aluru³⁹ (from CNT data) gives viscosity and friction coefficient results that differ significantly from graphene's. For instance, unlike CNT where viscosity tends to decrease with decreasing pore size and is predominantly below the bulk viscosity, graphene has a viscosity that increases with decreasing a and is above the bulk value. CNT CHP also significantly underestimates the friction coefficient, which means it would likely overestimate water permeance.

Table A1. Fitted parameters for thermophysical parameters, with pore radius a in nm.

Parameter	Units	Paper	Functional form	b_1	b_2	b_3
Viscosity μ	mPa s	Sun et al. (2021)	$b_2 e^{-b_1 a} + \mu_w$	2.29	0.00714	-
		Heiranian et al. <i>ACS Nano</i> . (2020)	$b_2 a^{b_3} e^{-b_1 a} + \mu_w$	4.75	0.231	3.81
Friction coefficient λ	mPa s nm ⁻¹	Sun et al. (2021)	$b_2 e^{-b_1 a} + b_3$	10.2	0.0151	0.00280
		Heiranian et al. <i>ACS Nano</i> . (2020)	$b_2 e^{-b_1 a} + b_3$	2.03	-0.000464	0.000708
Slip length δ_s	nm	Sun et al. (2021)	$\mu(a)/\lambda(a)$	-	-	-
		Heiranian et al. <i>ACS Nano</i> . (2020)	$b_2 e^{-b_1 a} + b_3$	2.42	4.88	2.44
		Heiranian et al. <i>Phys. Rev. Res.</i> (2020)	$b_2 e^{-b_1 a} + b_3$	1.10	4.48	1.26

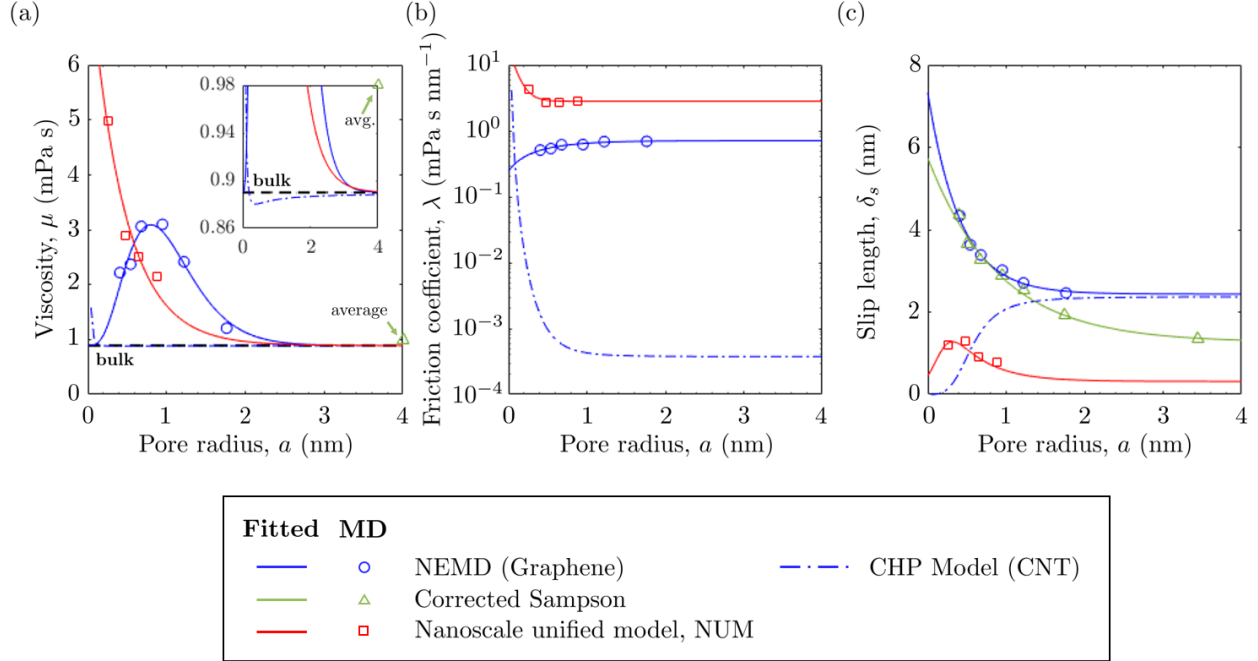


Figure A1. Graphene permeance calculated using Sampson (solid) and slip-and-viscosity-corrected Sampson (dash) flow models, using a graphene pore density value ρ_g of 10^{16} m^{-2} .

8.2.2 Results

The water permeances estimated using the slip-and-viscosity corrected Sampson, the corrected Hagen-Poiseuille (CHP; both CNT and graphene), and nanoscale unified model (NUM) are compared against that obtained using the simple Sampson model (**Figure A2**). The shapes of the curves are generally the same. Surprisingly, the NUM model gives results that are not significantly different from the Sampson model, perhaps because, while slip length increases with smaller pore radius (making flow faster), viscosity also increases (making flow slower), and the two effects likely balance each other out. The difference between the corrected and uncorrected permeances is less than one order of magnitude, suggesting that the use of the Sampson equation in our analysis should still yield reasonable estimates for permeance and selectivity with less complexity and generalizability to other materials. We expect the more accurate models with slippage would shift the water permeance and flux curves in **Figures 1a,d, 3, 4a,d, 6c** upwards by less than a magnitude (since at high fluxes the support resistance would be limiting), and the phase portrait curves to the right in **Figures 2, 5, 7**. The general conclusions drawn from this study about the effect of PSDs would remain the same. Nevertheless, as more theoretical models are generated and validated by experimental evidences, our analysis could be updated with the more accurate model(s), though the computational requirement could be higher.

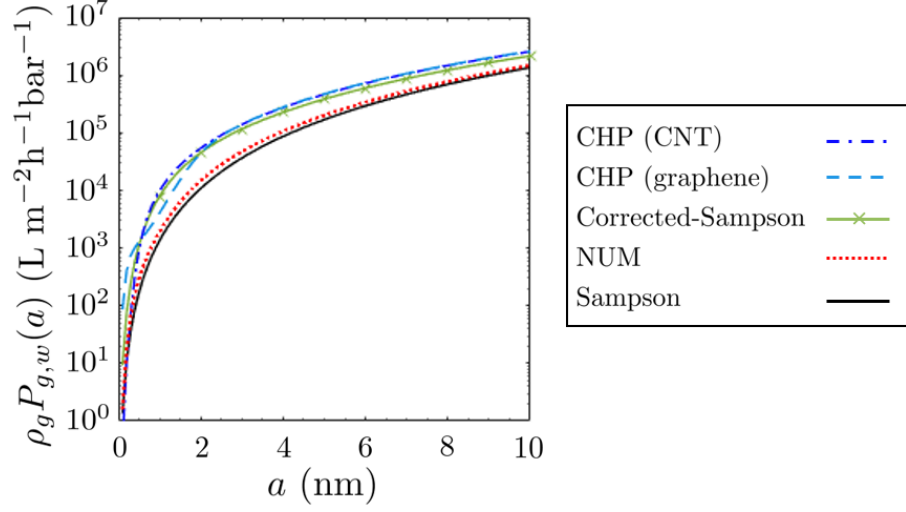


Figure A2. Graphene water permeance calculated using different flow models and a graphene pore density value ρ_g of 10^{16} m^{-2} : Sampson (solid), Sun et al.'s nanoscale unified model (NUM) with our fitted functions for viscosity and slip length (dotted),⁴⁰ Heiranian et al.'s slip-and-viscosity-corrected Sampson,³⁷ Heiranian and Aluru's corrected Hagen-Poiseuille (CHP) with our fitted functions for graphene (dash), and Heiranian and Aluru's CHP model with their fitted functions using CNT data (dot-dash).³⁹

8.3 Sample pore size distributions

Practical nanoporous graphene has pores that are spread across different sizes. Lognormal distributions are often used to describe pore sizes generated via top-down pore creation methods such as focused ion beam and oxidative etching.^{18,26,41} The mean and standard deviation in log-space is given by m and s , with e^m being the median in linear space.

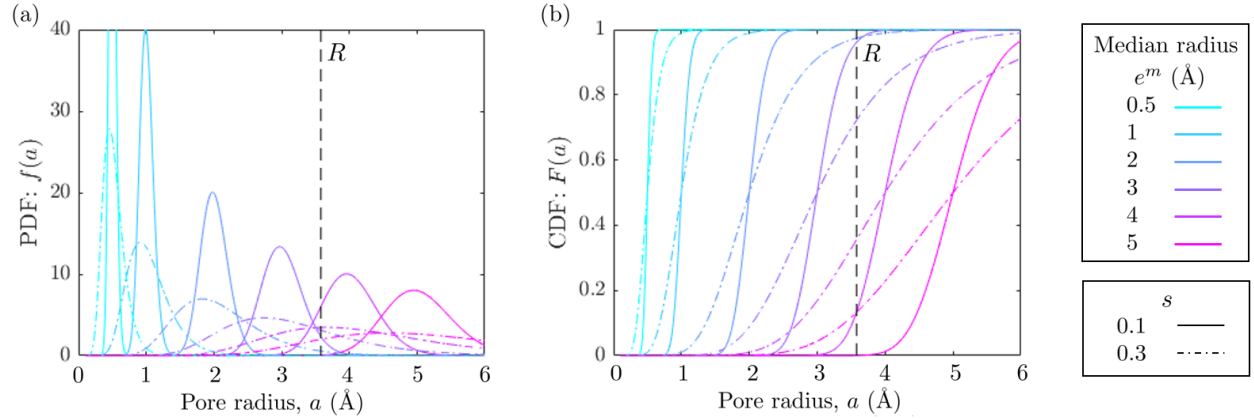


Figure A3. Lognormal PSDs. (a) Probability density function, (b) Cumulative distribution function for sample pore size distributions with different medians e^m and log-space standard deviations s . R is the hydrated ion size for Na^+ .

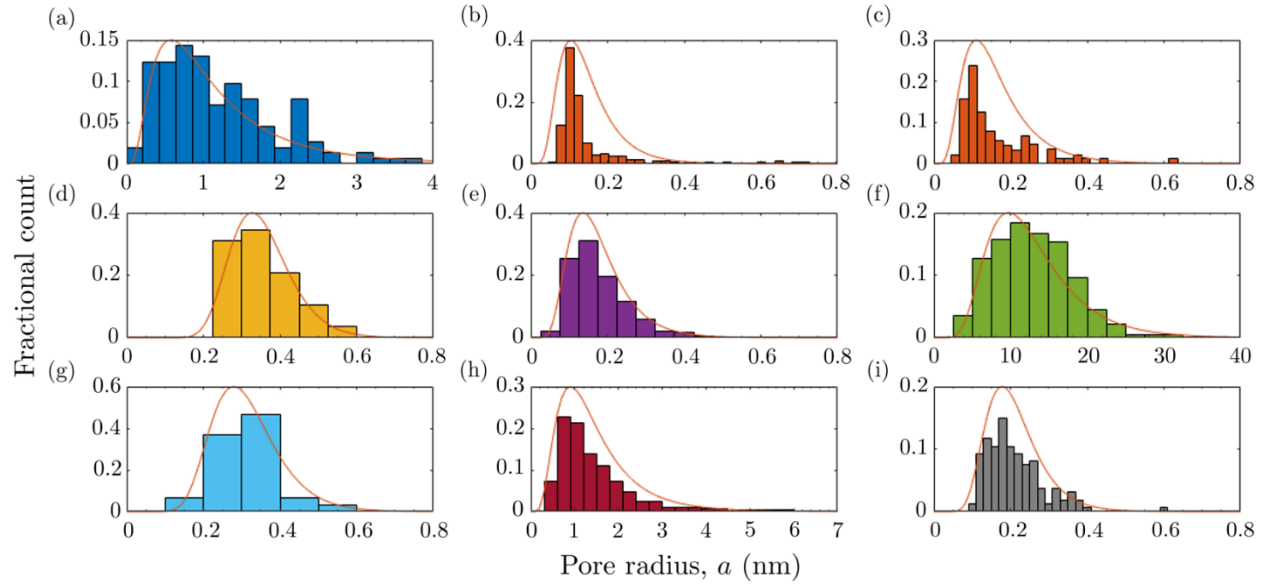


Figure A4. Pore size distributions in monolayer nanoporous graphene (a-g) and MoS_2 (h-i) from different experimental studies (bars), and the fitted lognormal probability density function (orange curves; scaled vertically to facilitate comparison). (a) He et al.⁶² 4 s O_2 plasma etch. (b) Jang et al.¹⁸ gallium ion irradiation (bombardment) followed by 50 s O_2 plasma etch; (c) 30 s O_2 plasma etch without ion irradiation. (d) Kidambi et al.⁴² 75 s O_2 plasma etch. (e) O'Hern et al.²⁶ gallium ion irradiation followed by 25 min $\text{KMnO}_4/\text{H}_2\text{SO}_4$ etch. (f) Wyss et al.⁴³ spherical block copolymer (s-BCP) based patterning with O_2 plasma etch. (g) Yang et al.¹⁹ meso-porous SiO_2 film with 10 s O_2 plasma etch. (h) Macha et al.⁶³ Xe ion irradiation. (i) Thiruraman et al.³¹ Ga^+ ion irradiation.

8.4 Energy barrier and its effect on transport rate

The presence of an energy barrier can affect salt transport across nanopores. **Figure A5** shows the energy barrier (normalized by thermal energy $k_B T$) and the exponential factor that modifies the transport rate as functions of pore size. As expected, as pore size increases, the average distance between any salt ion and the pore edge increases, and the water within the pores acts more similarly as the bulk, leading to a decrease in the energy barrier for interactions that are repulsive. The k_E values examined can describe molecular dynamics simulation data on the relationship between energy barrier and pore size fairly well. The data were taken from a literature review which compiled the activation energy barriers for the transport of various monovalent salts across different membrane structures and materials (e.g. nanoslits, nanopores of various lengths and sizes; graphene oxide, porous graphene, carbon nanotubes, other hydrophobic pores, etc.).⁴⁹ The energy barrier approaches 0 as pore size increases, leading to an exponential factor of 1 (no effect on salt transport).

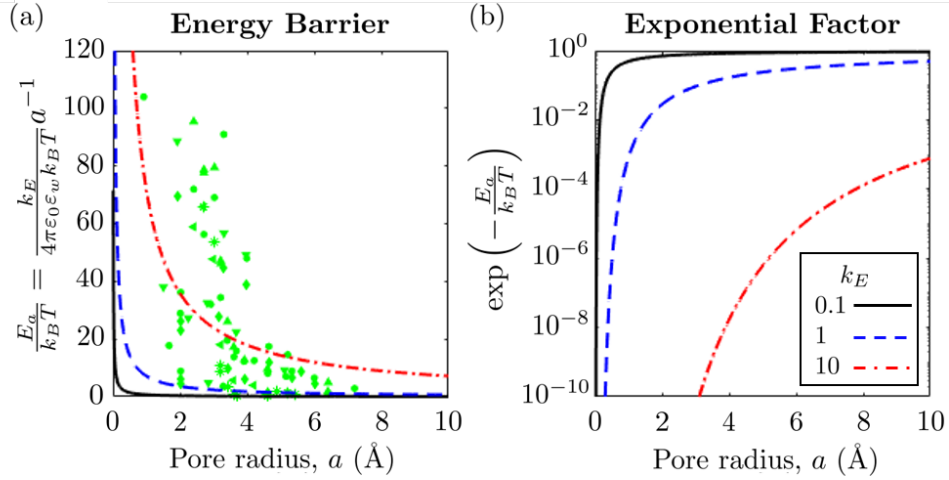


Figure A5. Effect of pore size on the energy barrier and the resulting exponential factor for salt transport, parametrized by $k_E = 0.1$ (solid lines), 1 (dash lines), and 10 (dot-dash lines). (a) Energy barrier versus pore radius. The energy barriers of various monovalent salt ions (represented by green symbols of different shapes) taken from molecular dynamics simulations for carbon nanotubes, graphene oxide membranes, porous graphene, and other hydrophobic pores are presented for comparison.⁴⁹ (b) Exponential term versus pore radius.

8.5 Concentration polarization

In the main text, we focused on the membrane property and thus did not consider concentration polarization, which typically occurs when water flux and salt rejection is high, causing build-up of salt on the feed side of the membrane at a higher concentration (by a factor of e^{J_w/k_f}) than the bulk feed. This in turn increases the osmotic pressure $\Delta\pi_m \propto \Delta c_m$ to be overcome in order to push water across the membrane, which decreases water flux ($J_w \propto (\Delta p - \Delta c_m)$) and increases salt concentration in the permeate, since there is less water to dilute the permeate salt solution.

However, in the case where convection is a substantial contributor to salt transport and salt rejection is not high, no substantial build-up of salt will occur on the feed side as the salt is transported across the membrane by the water flow. As shown in our analysis, high water fluxes, J_w , are typically associated with high convective salt transport due to the tails of the PSDs. In these situations, we have $\xi_{g,w} \rightarrow 1$ and $J_w \gg k_f$, where $k_f = 100 \text{ L m}^{-2} \text{ h}^{-1}$ is the overall feed side mass transfer coefficient, such that only the e^{J_w/k_f} terms survive in the salt balance:

$$\begin{aligned}
 J_w c_p &= J_s = \xi_{g,w} P_w \Delta p \left[1 + \left(1 - \frac{J_w}{\Delta p P_w} \right) \left(\frac{\phi_s \rho_g P_{g,w}^{tot}}{P_{supp,w}} \right) \right] [(c_{f,b} - c_p) e^{J_w/k_f} + c_p] + P_{diff} (c_{f,b} - c_p) e^{J_w/k_f} \\
 &\xrightarrow{J_w \gg k_f} 0 = \xi_{g,w} P_w \left[\Delta p + (1 - \xi_{g,w}) \Delta \pi_m \left(\frac{\phi_s \rho_g P_{g,w}^{tot}}{P_{supp,w}} \right) \right] (c_{f,b} - c_p) + P_{diff} (c_{f,b} - c_p) \\
 &\xrightarrow{\xi_{g,w} \rightarrow 1} 0 \approx J_w (c_{f,b} - c_p) + P_{diff} (c_{f,b} - c_p) \\
 &\xrightarrow{\xi_{g,w} \rightarrow 1} J_w c_p \approx J_w c_{f,b} + P_{diff} (c_{f,b} - c_p)
 \end{aligned}$$

We recover the governing for the case *without* concentration polarization for such a system since for high leakage $J_w \approx J_w^{a>R}$.

8.5.1 Results

The water and salt fluxes and permeate concentrations for the concentration polarization (CP) case can be determined via eq. (25), (27), and (29), using a typical overall feed side mass transfer coefficient k_f of $100 \text{ L m}^{-2} \text{ h}^{-1}$.¹¹ **Figures A6-7** present the results. CP only affects the curves in **Figure A6c-f**.

At high s values, i.e. when the spread of the PSD is large, or for median pore radii e^m of 4 and 5 Å that are larger than the salt radius, the PSD allows salt ions can leak through. Hence, the convective salt leakage is high and the CP curves for permeate concentration c_p , water flux J_w , and overall salt permeance $P_s = J_s/c_{f,b}$, $J_s = J_w c_p$, overlap with the no CP curves due to the large convective salt leakage and low salt rejection.

The effect of CP is also not as significant at low e^m and smaller values of s , since the water flux in the absence of CP is below the overall feed side mass transfer coefficient k_f of $100 \text{ L m}^{-2} \text{ h}^{-1}$ and as a result the rate of convective salt transport to the membrane surface is slow so there is effectively little CP.

At low s or smaller e^m , CP can lower the water flux J_w by increasing osmotic pressure, as salt transport across the membrane is slow (**Figures A6d**). However, this occurs only for PSDs with median radii e^m slightly below that of salt (2 and 3 Å) and to some extent for smaller e^m with slightly larger values of s that have moderate salt rejection and water flux in the absence of CP comparable to or higher than the k_f . Here, the permeate salt concentrations are higher (i.e., salt rejection is lower) as seen in **Figure A6c**. In these cases, CP increases the permeate concentration c_p by (i) elevating the salt concentration at the membrane surface of the feed, which increases the convective driving force, and (ii) reducing water flux, which decreases the dilution of the permeate (**Figures A6c**).

Since the overall salt flux J_s is the product of J_w and c_p and overall effective salt permeance P_s is just J_s scaled by a constant $c_{f,b}$, CP curves only deviate slightly from the no CP curves for overall salt permeance at intermediate s for intermediate e^m , where P_s with CP is slightly lower (**Figures A6e**). With CP, the diffusive contribution to salt flux increases with its peak shifting to lower s because of the high osmotic pressure that arises from higher concentration gradient across the membrane $\Delta c_m = c_{f,m} - c_p$ when water flux is low, yet the same Δc_m also drives salt diffusion (**Figures A6f**). The diffusive contribution rapidly decreases as s increase because with salt leakage the concentration gradient Δc_m vanishes, and convection drives most of the salt transport.

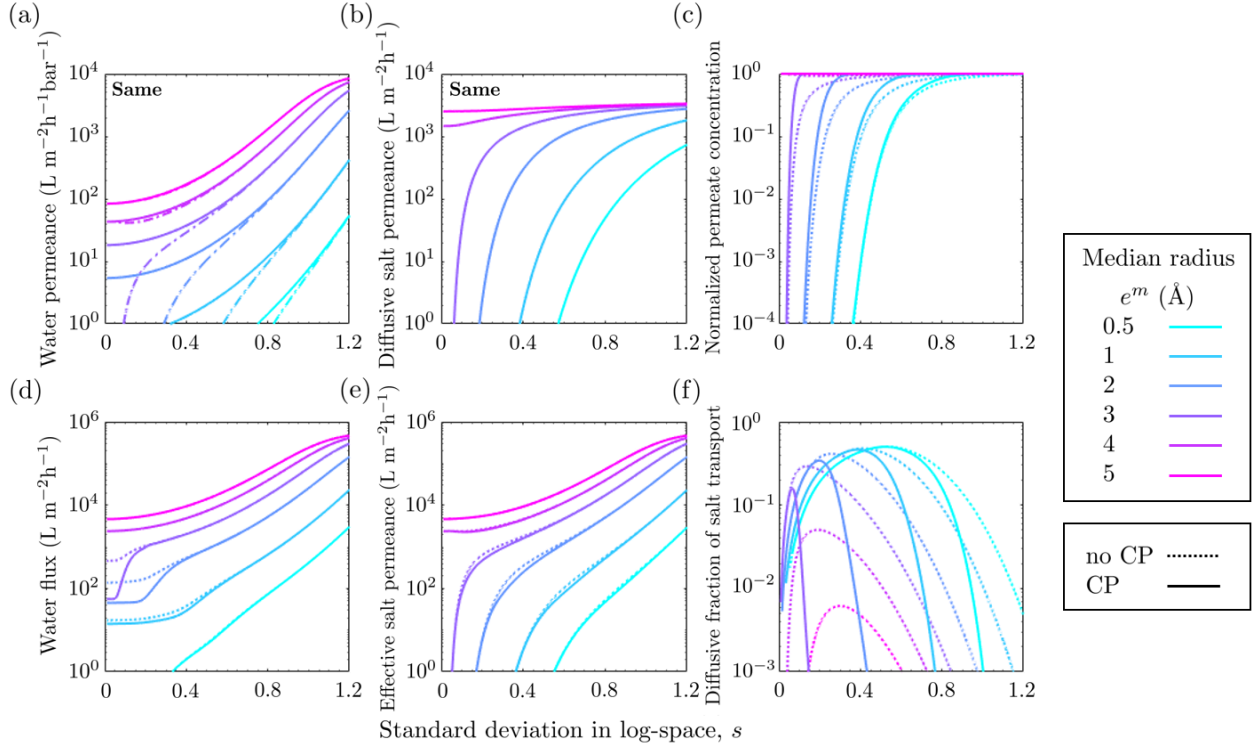


Figure A6. Case with concentration polarization (CP): Effect of log-space standard deviation of lognormal PSDs, s (x -axis), and median pore radii e^m (denoted by different colors), on water and salt transport across the membrane. (a-b) are the same for models with (CP) and without (no CP) concentration polarization incorporated. For (c-f), the solid vs. dotted curves refer to CP and no CP, respectively. (a) Water permeance P_w (solid lines) and water permeance for pores larger than the salt $P_w^{a>R}$ (dot-dash lines). (b) Diffusive salt permeance P_{diff} . (c) Permeate salt concentration normalized by the feed concentration $\tilde{c}_p = c_p/c_f$. (d) Water flux, J_w . (e) Overall effective salt permeance, $P_s \equiv J_s/c_f$. (f) Diffusive fraction of the total salt flux J_{diff}/J_s .

Similarly, the effect of concentration polarization on the phase plot curves is minimal (**Figure A7b-d**). Most of the curves in the region of interest (low permeate concentration; high salt rejection) are identical between CP and no CP.

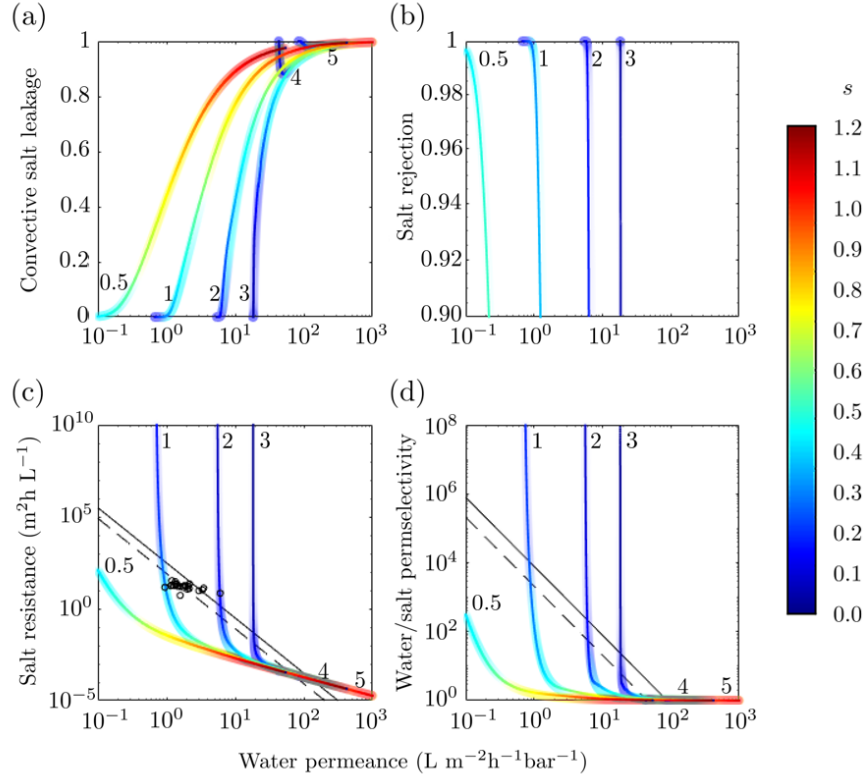


Figure A7. Case with concentration polarization (CP): Phase portraits of the trade-off between different measures of salt transport against the water permeance P_w (x -axis) for different lognormal PSDs characterized by median pore radii e^m (values in Å indicated next to each curve) and standard deviation in log-space, s (denoted by color). (a) is the same for models with and without CP. (b-d): the thin solid curves represent “CP”; the thick lighter transparency curves represent “no CP” for reference. The color indicates the log-space standard deviation of the PSD, s . (a) Convective salt leakage, $P_w^{a>R}/P_w$. (b) Salt rejection, $\mathcal{R} = 1 - c_p/c_f$. (c) Salt resistance (inverse of the effective salt permeance, P_s). The black dots denote commercial seawater RO membranes based on manufacturer technical specifications.¹¹ (d) Water/salt permselectivity, given by the ratio of the water flux to the salt permeance ($J_w/P_s = c_f/c_p$). The dash and solid black lines in (c-d) correspond to the empirically-determined and proposed upper bound permeance/selective trade-off curves for the membrane active layer of state-of-the-art, thin-film composite polyamide membranes.^{11,59}

8.5.2 Pore sealing

For pore sealing where the cut-off radii for the seals are smaller than the salt ion size, $R_{cap} < R$, there is no salt transport, and we expect concentration polarization to lower water flux by increasing osmotic pressure. Setting $c_p = 0$ in the water flux equation, i.e. $\Delta c_m = c_{f,m}$, gives:

$$\begin{aligned} J_w &= P_w(\Delta p - iR_g T c_{f,b} e^{J_w/k_f}) \\ \frac{J_w}{P_w \Delta p} &= \left(1 - \frac{iR_g T c_{f,b}}{\Delta p} e^{J_w/k_f}\right) \\ J_w &= P_w \Delta p - k_f W \left(\frac{iR_g T c_{f,b} P_w}{k_f} e^{\frac{P_w \Delta p}{k_f}} \right) \end{aligned} \quad (36)$$

where W is the product log/ Lambert W function.

Figure A8 shows the resulting water fluxes. Compared to no CP, CP curves are all shifted lower, especially the PSDs with the highest fluxes ($e^m = 2, 3$ nm) because their concentration polarization is also the most severe as $c_{f,m} = c_{f,b} e^{J_w/k_f}$. The rest of the trends are the same between no CP and CP. Furthermore, because higher water fluxes are associated with higher concentration polarization, i.e. higher feed salt concentration at the membrane surface and thus higher osmotic pressure opposing the water flow, one can reduce the applied pressure without affecting water fluxes much, resulting in energy savings (**Figure A8**).

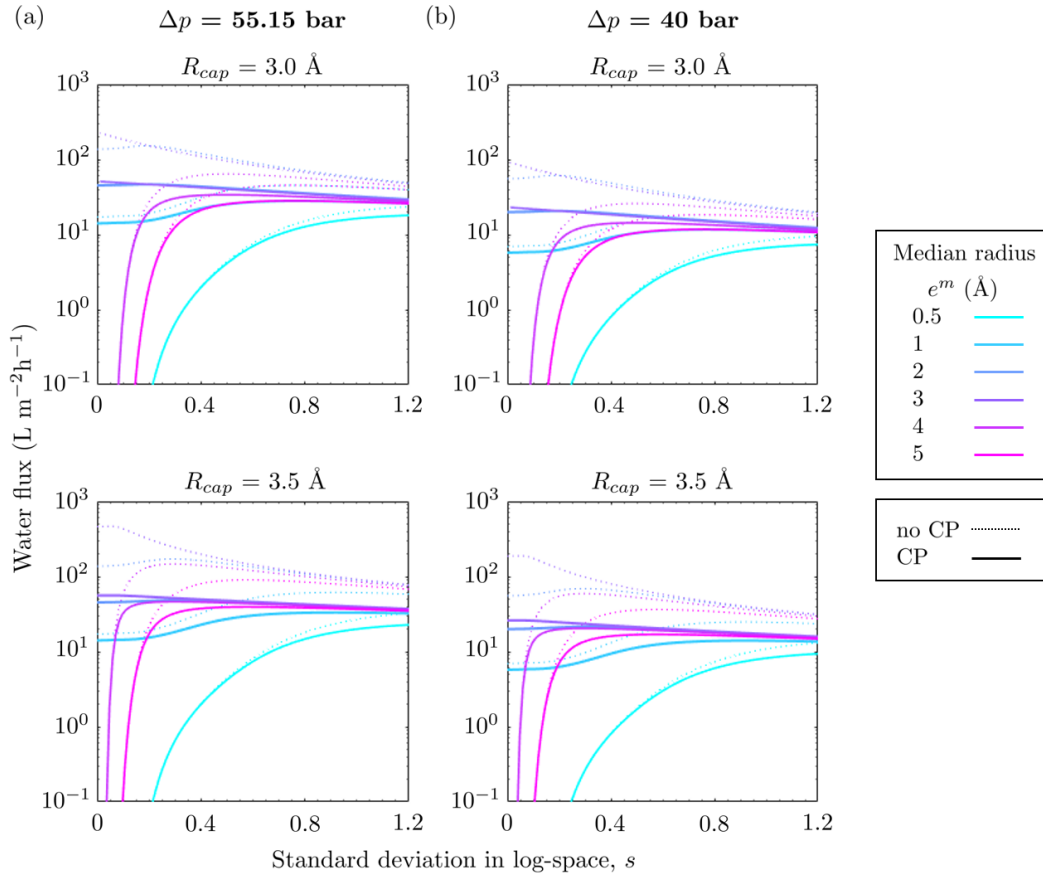


Figure A8. Case with concentration polarization (CP): Water flux J_w as a function of standard deviation in log-space s for different applied pressure Δp of (a) 55.15 and (b) 40 bar, and different

sealing cut-offs, $R_{cap} = 3.0 \text{ \AA}$ (top) and $R_{cap} = 3.5 \text{ \AA}$ (bottom), both of which are smaller than the salt ion radius $R = 3.58 \text{ \AA}$. There is no salt transport since both cut-off values are below the salt ion size. The solid vs. dotted curves refer to CP and no CP, respectively.

9. Literature Citations

1. Sedlak, D. L. *Water 4.0: The Past, Present, and Future of the World's Most Vital Resource*. (Yale University Press, 2015).
2. Elimelech, M. & Phillip, W. A. The Future of Seawater and the Environment. *Science* (1979) **333**, 712–717 (2011).
3. Geise, G. M., Park, H. B., Sagle, A. C., Freeman, B. D. & McGrath, J. E. Water permeability and water/salt selectivity tradeoff in polymers for desalination. *J Memb Sci* **369**, 130–138 (2011).
4. Jiang, C. *et al.* Ultrathin Film Composite Membranes Fabricated by Novel In Situ Free Interfacial Polymerization for Desalination. *ACS Appl Mater Interfaces* **12**, 25304–25315 (2020).
5. Liu, J., Wang, Z., Li, W., Wang, X. & Su, Y. Graphene quantum dots enhanced ultrathin nanofilms and arginine engineered nanofiltration membranes with ultra-high separation performance. *Desalination* **547**, 116232 (2023).
6. Cohen-Tanugi, D. & Grossman, J. C. Water desalination across nanoporous graphene. *Nano Lett* **12**, 3602–3608 (2012).
7. Mauter, M. S. *et al.* The role of nanotechnology in tackling global water challenges. *Nat Sustain* **1**, 166–175 (2018).
8. O'Hern, S. C. *et al.* Selective molecular transport through intrinsic defects in a single layer of CVD graphene. *ACS Nano* **6**, 10130–10138 (2012).
9. Surwade, S. P. *et al.* Water desalination using nanoporous single-layer graphene. *Nat Nanotechnol* **10**, 459–464 (2015).
10. Cohen-Tanugi, D., McGovern, R. K., Dave, S. H., Lienhard, J. H. & Grossman, J. C. Quantifying the potential of ultra-permeable membranes for water desalination. *Energy Environ Sci* **7**, 1134–1141 (2014).
11. Werber, J. R., Deshmukh, A. & Elimelech, M. The Critical Need for Increased Selectivity, Not Increased Water Permeability, for Desalination Membranes. *Environ Sci Technol Lett* **3**, 112–120 (2016).
12. Wang, L., Williams, C. M., Boutilier, M. S. H., Kidambi, P. R. & Karnik, R. Single-Layer Graphene Membranes Withstand Ultrahigh Applied Pressure. *Nano Lett* **17**, 3081–3088 (2017).
13. Wang, L. *et al.* Fundamental transport mechanisms, fabrication and potential applications of nanoporous atomically thin membranes. *Nat Nanotechnol* **12**, 509–522 (2017).
14. Cohen-Tanugi, D. & Grossman, J. C. Nanoporous graphene as a reverse osmosis membrane: Recent insights from theory and simulation. *Desalination* **366**, 59–70 (2015).

15. Suk, M. E. & Aluru, N. R. Molecular and continuum hydrodynamics in graphene nanopores. *RSC Adv* **3**, 9365–9372 (2013).
16. Suk, M. E. & Aluru, N. R. Ion transport in sub-5-nm graphene nanopores. *Journal of Chemical Physics* **140**, (2014).
17. Cheng, P. *et al.* Facile Size-Selective Defect Sealing in Large-Area Atomically Thin Graphene Membranes for Sub-Nanometer Scale Separations. *Nano Lett* **20**, 5951–5959 (2020).
18. Jang, D., Idrobo, J. C., Laoui, T. & Karnik, R. Water and Solute Transport Governed by Tunable Pore Size Distributions in Nanoporous Graphene Membranes. *ACS Nano* **11**, 10042–10052 (2017).
19. Yang, Y. *et al.* Large-area graphene-nanomesh/carbon-nanotube hybrid membranes for ionic and molecular nanofiltration. *Science (1979)* **1062**, 1057–1062 (2019).
20. O’Hern, S. C. *et al.* Nanofiltration across defect-sealed nanoporous monolayer graphene. *Nano Lett* **15**, 3254–3260 (2015).
21. Boutilier, M. S. H. *et al.* Molecular Sieving Across Centimeter-Scale Single-Layer Nanoporous Graphene Membranes. *ACS Nano* **11**, 5726–5736 (2017).
22. Faucher, S. *et al.* Critical Knowledge Gaps in Mass Transport through Single-Digit Nanopores: A Review and Perspective. *Journal of Physical Chemistry C* **123**, 21309–21326 (2019).
23. Wang, L. *et al.* Salt and Water Transport in Reverse Osmosis Membranes: Beyond the Solution-Diffusion Model. *Environ Sci Technol* **55**, 16665–16675 (2021).
24. Hegde, V. H., Doherty, M. F. & Squires, T. M. A two-phase model that unifies and extends the classical models of membrane transport. *Science (1979)* **377**, 186–191 (2022).
25. Atwal, H. K., Wong, A. O. K. & Boutilier, M. S. H. Mass Advection-Diffusion in Creeping Flow Through an Orifice Plate: A Model for Nanoporous Atomically Thin Membranes. *J Heat Transfer* **144**, (2022).
26. O’Hern, S. C. *et al.* Selective ionic transport through tunable subnanometer pores in single-layer graphene membranes. *Nano Lett* **14**, 1234–1241 (2014).
27. Sun, C. *et al.* Mechanisms of molecular permeation through nanoporous graphene membranes. *Langmuir* **30**, 675–682 (2014).
28. Bondaz, L., Chow, C. M. & Karnik, R. Rapid screening of nanopore candidates in nanoporous single-layer graphene for selective separations using molecular visualization and interatomic potentials. *Journal of Chemical Physics* **154**, 1–11 (2021).
29. de Souza, J. P., Chow, C. M., Karnik, R. & Bazant, M. Z. Nonlinear ion transport mediated by induced charge in ultrathin nanoporous membranes. *Phys Rev E* **104**, (2021).

30. Jain, T. *et al.* Heterogeneous sub-continuum ionic transport in statistically isolated graphene nanopores. *Nat Nanotechnol* **10**, 1053–1057 (2015).
31. Thiruraman, J. P. *et al.* Angstrom-Size Defect Creation and Ionic Transport through Pores in Single-Layer MoS₂. *Nano Lett* **18**, 1651–1659 (2018).
32. Rollings, R. C., Kuan, A. T. & Golovchenko, J. A. Ion selectivity of graphene nanopores. *Nat Commun* **7**, (2016).
33. Babu, C. S. & Lim, C. Theory of Ionic Hydration: Insights from Molecular Dynamics Simulations and Experiment. *J Phys Chem B* **103**, 7958–7968 (1999).
34. Bankura, A., Carnevale, V. & Klein, M. L. Hydration structure of salt solutions from *ab initio* molecular dynamics. *J Chem Phys* **138**, 014501 (2013).
35. Fu, Y. *et al.* Dehydration-Determined Ion Selectivity of Graphene Subnanopores. *ACS Appl Mater Interfaces* **12**, 24281–24288 (2020).
36. Sahu, S., di Ventra, M. & Zwolak, M. Dehydration as a Universal Mechanism for Ion Selectivity in Graphene and Other Atomically Thin Pores. *Nano Lett* **17**, 4719–4724 (2017).
37. Heiranian, M., Taqieddin, A. & Aluru, N. R. Revisiting Sampson’s theory for hydrodynamic transport in ultrathin nanopores. *Phys Rev Res* **2**, (2020).
38. Jensen, K. H., Valente, A. X. C. N. & Stone, H. A. Flow rate through microfilters: Influence of the pore size distribution, hydrodynamic interactions, wall slip, and inertia. *Physics of Fluids* **26**, (2014).
39. Heiranian, M. & Aluru, N. R. Nanofluidic Transport Theory with Enhancement Factors Approaching One. *ACS Nano* **14**, 272–281 (2020).
40. Sun, C., Zhou, R., Zhao, Z. & Bai, B. Extending the Classical Continuum Theory to Describe Water Flow through Two-Dimensional Nanopores. *Langmuir* **37**, 6158–6167 (2021).
41. Dutta, S., Vahdat, M. T., Rezaei, M. & Agrawal, K. V. Crystallization of gas-selective nanoporous graphene by competitive etching and growth: a modeling study. *Sci Rep* **9**, (2019).
42. Kidambi, P. R. *et al.* Nanoporous Atomically Thin Graphene Membranes for Desalting and Dialysis Applications. *Advanced Materials* **29**, 1–8 (2017).
43. Wyss, R. M., Tian, T., Yazda, K., Park, H. G. & Shih, C. J. Macroscopic Salt Rejection through Electrostatically Gated Nanoporous Graphene. *Nano Lett* **19**, 6400–6409 (2019).
44. Chow, C.-M. Nanoporous graphene membranes for health and environmental applications. (Massachusetts Institute of Technology, 2023).

45. Lu, Y. *et al.* Monolayer graphene membranes for molecular separation in high-temperature harsh organic solvents. *Proceedings of the National Academy of Sciences* **118**, (2021).
46. Boutilier, M. S. H. *et al.* Implications of permeation through intrinsic defects in graphene on the design of defect-tolerant membranes for gas separation. *ACS Nano* **8**, 841–849 (2014).
47. Cheng, C., Iyengar, S. A. & Karnik, R. Molecular size-dependent subcontinuum solvent permeation and ultrafast nanofiltration across nanoporous graphene membranes. *Nat Nanotechnol* **16**, 989–995 (2021).
48. Han, J., Fu, J. & Schoch, R. B. Molecular sieving using nanofilters: Past, present and future. *Lab on a Chip* vol. 8 23–33 Preprint at <https://doi.org/10.1039/b714128a> (2007).
49. Epsztein, R., DuChanois, R. M., Ritt, C. L., Noy, A. & Elimelech, M. Towards single-species selectivity of membranes with subnanometre pores. *Nat Nanotechnol* **15**, 426–436 (2020).
50. Yaroshchuk, A., Bruening, M. L. & Zholkovskiy, E. Modelling nanofiltration of electrolyte solutions. *Advances in Colloid and Interface Science* vol. 268 39–63 Preprint at <https://doi.org/10.1016/j.cis.2019.03.004> (2019).
51. Hennequin, T., Manghi, M. & Palmeri, J. Competition between Born solvation, dielectric exclusion, and Coulomb attraction in spherical nanopores. *Phys Rev E* **104**, 44601 (2021).
52. Fievet, P. Donnan Steric Pore (DSP) and Dielectric Exclusion (DE) Model. in *Encyclopedia of Membranes* 1–5 (Springer Berlin Heidelberg, 2014). doi:10.1007/978-3-642-40872-4_1717-1.
53. Silva, V. Dielectric Exclusion Model in Membranes. in *Encyclopedia of Membranes* 1–3 (Springer Berlin Heidelberg, 2015). doi:10.1007/978-3-642-40872-4_1888-1.
54. Aragones, J. L., MacDowell, L. G. & Vega, C. Dielectric Constant of Ices and Water: A Lesson about Water Interactions. *Journal of Physical Chemistry A* **115**, 5745–5758 (2011).
55. Hennequin, T., Manghi, M. & Palmeri, J. Competition between Born solvation, dielectric exclusion, and Coulomb attraction in spherical nanopores. *Phys Rev E* **104**, 044601 (2021).
56. Zhu, H. *et al.* Investigation of dielectric constants of water in a nano-confined pore. *RSC Adv* **10**, 8628–8635 (2020).
57. Rickhaus, P. *et al.* The electronic thickness of graphene. *Sci. Adv* vol. 6 <https://www.science.org> (2020).
58. Fang, J., Vandenberghe, W. G. & Fischetti, M. v. Microscopic dielectric permittivities of graphene nanoribbons and graphene. *Phys Rev B* **94**, (2016).

59. Yip, N. Y. & Elimelech, M. Performance limiting effects in power generation from salinity gradients by pressure retarded osmosis. *Environ Sci Technol* **45**, 10273–10282 (2011).
60. Heiranian, M., Farimani, A. B. & Aluru, N. R. Water desalination with a single-layer MoS₂ nanopore. *Nat Commun* **6**, 8616 (2015).
61. Dagan, Z., Weinbaum, S. & Pfeffer, R. An infinite-series solution for the creeping motion through an orifice of finite length. *J Fluid Mech* **115**, 505–523 (1982).
62. He, G. *et al.* High-permeance polymer-functionalized single-layer graphene membranes that surpass the postcombustion carbon capture target. *Energy Environ Sci* **12**, 3305–3312 (2019).
63. Macha, M. *et al.* High-Throughput Nanopore Fabrication and Classification Using Xe-Ion Irradiation and Automated Pore-Edge Analysis. *ACS Nano* **16**, 16249–16259 (2022).